Article

Cell Reports

FMRP Control of Ribosome Translocation Promotes Chromatin Modifications and Alternative Splicing of Neuronal Genes Linked to Autism

Graphical Abstract

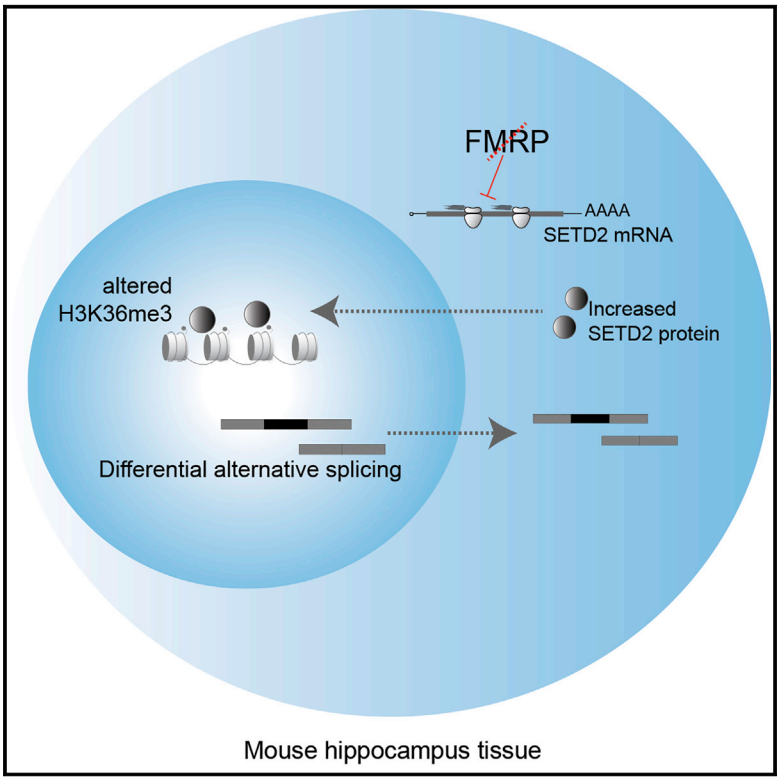

Highlights

- Loss of FMRP reduces ribosome stalling on specific mRNAs, including Setd2
- Increased SETD2 protein alters H3K36me3 marks in FMRP-deficient hippocampus
- Alternative splicing is dysregulated in FMRP-deficient hippocampus
- Altered H3K36me3 and splicing occur on genes and transcripts linked to autism

Authors

Sneha Shah, Gemma Molinaro, Botao Liu, Ruijia Wang, Kimberly M. Huber, Joel D. Richter

Correspondence

kimberly.huber@utsouthwestern.edu (K.M.H.), joel.richter@umassmed.edu (J.D.R.)

In Brief

Shah et al. show that many neuronal mRNAs are associated with FMRP-stalled ribosomes. FMRP-regulated ribosome stalling influences the chromatin landscape. These events in turn mediate alternative processing of pre-mRNAs linked to autism.

Shah et al., 2020, Cell Reports *30*, 4459–4472
March 31, 2020
https://doi.org/10.1016/j.celrep.2020.02.076

CellPress

Cell Reports
Article

FMRP Control of Ribosome Translocation Promotes Chromatin Modifications and Alternative Splicing of Neuronal Genes Linked to Autism

Sneha Shah,[1,3] Gemma Molinaro,[2,3] Botao Liu,[1,3] Ruijia Wang,[1] Kimberly M. Huber,[2,*] and Joel D. Richter[1,4,*]
[1]Program in Molecular Medicine, University of Massachusetts Medical School, Worcester, MA 01605, USA
[2]Department of Neuroscience, University of Texas Southwestern Medical School, Dallas, TX 75390, USA
[3]These authors contributed equally
[4]Lead Contact
*Correspondence: kimberly.huber@utsouthwestern.edu (K.M.H.), joel.richter@umassmed.edu (J.D.R.)
https://doi.org/10.1016/j.celrep.2020.02.076

SUMMARY

Silencing of *FMR1* and loss of its gene product, FMRP, results in fragile X syndrome (FXS). FMRP binds brain mRNAs and inhibits polypeptide elongation. Using ribosome profiling of the hippocampus, we find that ribosome footprint levels in *Fmr1*-deficient tissue mostly reflect changes in RNA abundance. Profiling over a time course of ribosome runoff in wild-type tissue reveals a wide range of ribosome translocation rates; on many mRNAs, the ribosomes are stalled. Sucrose gradient ultracentrifugation of hippocampal slices after ribosome runoff reveals that FMRP co-sediments with stalled ribosomes, and its loss results in decline of ribosome stalling on specific mRNAs. One such mRNA encodes SETD2, a lysine methyltransferase that catalyzes H3K36me3. Chromatin immunoprecipitation sequencing (ChIP-seq) demonstrates that loss of FMRP alters the deployment of this histone mark. H3K36me3 is associated with alternative pre-RNA processing, which we find occurs in an FMRP-dependent manner on transcripts linked to neural function and autism spectrum disorders.

INTRODUCTION

Fragile X syndrome (FXS) is characterized by intellectual disability, developmental delays, social impairment, and other maladies. The cause of FXS is an iteration of ~200 or more CGG triplets in *FMR1* that induces DNA methylation and transcriptional inactivation. Loss of the *FMR1* gene product FMRP results in synaptic dysfunction and aberrant circuit formation, which produces neuro-pathological conditions during development (Santoro et al., 2012). FXS is modeled in *Fmr1* knockout (KO) mice, which mimic many facets of the human disease, including learning and memory deficits, repetitive disorders, and susceptibility to seizures. In these animals, neuronal communication is frequently examined at hippocampal Schaffer collateral-CA1 synapses, which exhibit exaggerated metabotropic glutamate-receptor-dependent long-term depression (mGluR-LTD) (Huber et al., 2002). This form of synaptic plasticity normally requires protein synthesis, but in *Fmr1*-deficient animals, protein synthesis is both unnecessary for mGluR-LTD and excessive in neurons, which contributes to aberrant circuit formation and other hallmarks of the syndrome (Waung and Huber, 2009).

FMRP is an RNA-binding protein present in most cells; in neurons, its localization at postsynaptic sites is thought to control activity-dependent synapse remodeling by regulating mRNA expression (Richter et al., 2015). Considerable effort has been made to identify FMRP target mRNAs, but the most rigorous involves *in vivo* crosslink and immunoprecipitation (CLIP). CLIP combined with RNA sequencing (RNA-seq) has identified 842 target mRNAs in the post-natal day 11 (P11)–P25 mouse cortex and cerebellum (Darnell et al., 2011); predominantly a single mRNA in cultured cortical neurons (Tabet et al., 2016); 1,610 RNAs in the P13 cortex, hippocampus, and cerebellum (Maurin et al., 2018); and ~6,000 RNAs in HEK cells expressing epitope-tagged FMRP (Ascano et al., 2012). This diversity of FMRP CLIP targets could reflect the different procedures employed or the different brain cell types examined. Surprisingly, the majority of CLIP sites in mRNA are in coding regions (Darnell et al., 2011; Maurin et al., 2018), with a bias to some *cis* sequences (Anderson et al., 2016; Maurin et al., 2018). FMRP association with mRNA coding regions and co-sedimentation with polyribosomes (Khandjian et al., 1996; Feng et al., 1997; Stefani et al., 2004) suggests it normally inhibits translation by impeding ribosome translocation. Indeed, studies that examined polypeptide elongation (Udagawa et al., 2013) or susceptibility to puromycin release of nascent polypeptides (Darnell et al., 2011) indicate that FMRP regulates ribosome transit. Supporting evidence comes from studies showing that *Drosophila* FMRP interacts with ribosomal protein L5 (Ishizuka et al., 2002), which may preclude tRNA or elongation factors from engaging the ribosome and causing it to stall (Chen et al., 2014). Although these observations need to be extended to mammalian FMRP, they suggest a molecular mechanism by which FMRP stalls ribosomes. Such observations do not indicate how FMRP could stall ribosomes on specific mRNAs.

Ribosome profiling is a whole-transcriptome method for analyzing the number and positions of ribosomes associated with mRNA; when combined with RNA-seq, it yields heretofore unobtainable information on gene expression at high resolution

(Ingolia et al., 2009; Ingolia, 2014; Brar and Weissman, 2015). We used ribosome profiling to explore FMRP regulation of gene expression in mouse adult neural stems cells (aNSCs), which in FXS have a proclivity to differentiate into glia at the expense of neurons (Liu et al., 2018; Luo et al., 2010; Guo et al., 2011). We identified mRNAs whose ribosome occupancy was either up or downregulated in FMRP-deficient cells or had altered steady-state levels reflected by their association with ribosomes. We identified yet additional mRNAs whose ribosome occupancy was "buffered" so that changes in their levels were compensated for by opposite changes in ribosome association (Liu et al., 2018).

Ribosome profiling at steady state cannot distinguish between translocating and stalled ribosomes, suggesting that studies examining FMRP-regulated translation by this method or translating ribosome affinity purification (TRAP) and RNA-seq (TRAP-seq) (Thomson et al., 2017; Liu et al., 2018, 2019; Greenblatt and Spradling, 2018; Das Sharma et al., 2019) may overlook key events leading to FXS. Moreover, if intact brain circuitry is important for FMRP regulation, then cultured neurons might not reveal important aspects of FMRP function. To circumvent these issues, we have developed a hippocampal slice assay to detect mRNA-specific ribosome translocation dynamics. Hippocampal slices maintain the *in vivo* synaptic connectivity and cellular architecture and express protein synthesis and FMRP-dependent forms of synaptic plasticity (Huber et al., 2002). Profiling over a time course of ribosome runoff in slices demonstrates a wide range of ribosome translocation rates on specific mRNAs, from rapid (rates similar to those in embryonic stem [ES] cells; Ingolia et al., 2011) to near-complete stalling. Many mRNAs retain 4–6 ribosomes after runoff in wild-type (WT), but not in FMRP-deficient, slices. Some RNAs associated with FMRP-stalled ribosomes encode proteins involved in neurologic function and transcriptional regulation. One such RNA encodes SETD2, a methyltransferase for the chromatin mark H3K36me3. We find increased SETD2 protein in *Fmr1*-deficient hippocampus. Chromatin immunoprecipitation sequencing (ChIP-seq) demonstrates that distribution of this mark varies in a genotype (i.e., WT versus *Fmr1*-deficient)-dependent manner in hippocampal tissue. In mammals, apart from blocking cryptic transcription initiation and DNA damage response, H3K36me3 is correlated with pre-mRNA processing events such as alternative splicing (Kim et al., 2011; Kolasinska-Zwierz et al., 2009). RNA-seq reveals that splicing events such as exon skipping are altered in FMRP-deficient slices and that these transcripts are linked to neural function and autism spectrum disorders. Aberrant RNA splicing of synapse related genes is prevalent in autism spectrum disorders (Lee et al., 2016; Quesnel-Vallières et al., 2016; Smith and Sadee, 2011). Our study demonstrates that a reduction in ribosome stalling in the *Fmr1*-deficient brain results in a cascade of epigenetic and RNA processing changes that likely contribute to neurologic disease.

RESULTS

Hippocampal Schafer collateral-CA1 synapses exhibit an exaggerated mGluR-LTD in *Fmr1*-deficient mice that is aberrantly protein-synthesis independent (Nosyreva and Huber, 2006; Huber et al., 2000). To identify mRNAs whose basal expression is misregulated, we prepared CA1-enriched hippocampal slices (400 μm) (Figure 1A), performed ribosome profiling and RNA-seq (Figure 1B), and calculated translational efficiency (TE), the ratio of ribosome footprints to RNA-seq reads. We identified RNAs with changes in TE (TE up/TE down) or RNAs whose levels were elevated or reduced but without changes in TE (mRNA up/mRNA down) (Figure 1C; Table S1) (nominal p value < 0.01, false discovery rate [FDR] = 0.097 by permutation test). A Gene Ontology (GO) analysis of the biological processes most enriched in each group shows that the mRNA-down group encodes factors that mediate taxis/chemotaxis, while the mRNA-up group encodes factors involved in ribonucleotide metabolism (Figure 1D, S1A, and S1B). The TE-down mRNAs encode factors that control synaptic transmission (Figures 1D and S1C). The mRNA-down group is enriched for cellular components linked to the extracellular matrix, while the mRNA-up group encodes the myelin sheath and spliceosome-interacting factors. The TE-down group is involved in the extracellular matrix and synaptic architecture (Figures 1E and S1C). No GO terms from the TE-up group were statistically significant.

Heatmaps of the top 20 mRNAs with altered up and down TEs in *Fmr1*-deficient slices compared to the WT are shown in Figures 2A and 2B. Examples of the change in TEs are depicted in Figures 2C and 2D. *Gfpt2* (glutamine-fructose-6-phosphate transaminase 2) mRNA is nearly unchanged in *Fmr1* KO but has an increase in ribosome footprints; Figure 2C). Conversely *Lhfpl5* (lipoma high-mobility group protein isoform C [HMGIC] fusion partner-like 5) mRNA has reduced numbers of ribosome footprints while RNA levels are mostly unchanged (Figure 2D). Neither *Gfpt2* nor *Lhfpl5* mRNAs have FMRP CLIP sites. Figure 2E shows boxplots for all 843 FMRP CLIP RNAs (p value < 0.0001, Wilcoxon test) (Darnell et al., 2011). As a group, these RNAs decrease significantly in *Fmr1* KO, which is tracked by commensurate decreases in ribosome footprints resulting in no change in TE.

We compared our TE-down and TE-up groups in *Fmr1* KO hippocampus with results from Das Sharma et al. (2019), who performed ribosome profiling on mouse frontal cortex, and Thomson et al. (2017), who performed TRAP-seq from hippocampal CA1 pyramidal neurons (Figure 2F). Only 37 of our TE-down RNAs were detected by Das Sharma et al., 2019 (~7% overlap), and only 5 were detected by Thomson et al. (2017) (~17% overlap). Even fewer of our TE-up RNAs were detected in either of those studies (Figure 2F) (~2% overlap). We surmise that the differences in methods and source material are likely responsible for little overlap among the studies.

Our data show almost all changes in ribosome footprint number in *Fmr1*-deficient slices can be attributed to altered RNA levels irrespective of whether the transcripts are FMRP CLIP targets. This suggests that the increase in incorporation of labeled amino acids into protein in *Fmr1* KO hippocampal slices (e.g., Dölen et al., 2007; Udagawa et al., 2013; Bowling et al., 2019) is mostly due to changes in RNA levels and/or ribosome transit rate. However, TE may not necessarily reflect protein production. For example, increased initiation with no change in elongation would produce increased ribosome footprints and yield an elevated level of protein product (Figure 2G). If there is no change

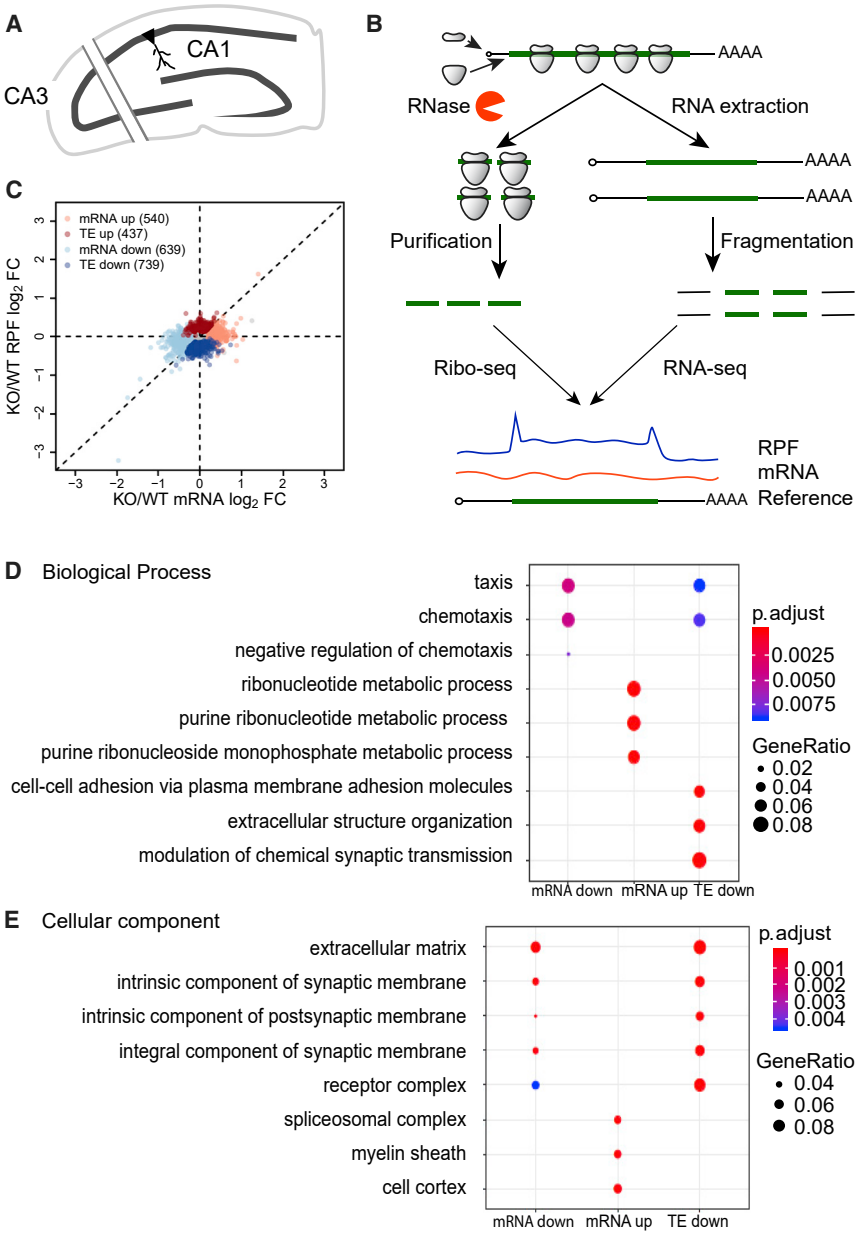

Figure 1. Ribosome Profiling Reveals Diverse Changes of Gene Expression in *Fmr1* KO Hippocampus

(A) Schematic diagram of the hippocampal slice preparation. To reduce spontaneous electrical activity, region CA3 was excised. 8–10 slices from six to eight mice/genotype were pooled per biological replicate (wild-type [WT], n = 4 and *Fmr1* KO, n = 3).

(B) Schematic diagram of the experimental procedures for ribosome profiling.

(C) Scatterplot of expression changes of mRNA levels and ribosome-protected fragments (RPFs). Dysregulated mRNAs in the absence of FMRP are classified into four regulatory groups. 14,459 genes past filtering are used for the scatterplot. Nominal $p < 0.01$, FDR = 0.097 by permutation test. FC, fold change; TE, translational efficiency.

(D) Top three GO terms of Biological Process enriched in each regulatory group. The enrichment (gene ratio) is represented by the size of dots. The enrichment significance (adjusted p value) is color-coded.

(E) Top three GO terms of Cellular Component enriched in each regulatory group.

See also Figure S1 and Table S1.

in initiation but elevated elongation, the TE will appear to be reduced but the production of protein will be increased. Consequently, ribosome profiling at steady state, which cannot distinguish between transiting and stalled ribosomes, may inadequately represent translation if there are changes in elongation. To assess whether FMRP regulates ribosome dynamics, we modified our procedure to investigate temporal changes in transcriptome-wide ribosome translocation rates.

Ribosome Runoff Dynamics in Hippocampal-Cortical Slices

We next performed ribosomal profiling and RNA-seq in hippocampal-cortical slices at different time points after blocking initiation with homoharringtonine (HHT). HHT halts ribosomes on initiation codons but allows elongating ribosomes to continue translocating until they run off (Ingolia et al., 2011; Lee et al., 2012). We aimed to determine differences in ribosome translocation rates of all expressed genes in WT tissue slices. Slices were incubated with HHT for 0–60 min and ribosome transit stopped at specific times with cycloheximide; the samples were then used for ribosome profiling (Figure 3A; Table S1). A metagene analysis of the ribosome footprints on 1,401 mRNAs with open reading frames (ORFs) of >3,000 nt aligned with the start and stop codons is shown in Figure 3B, indicating that the ribosomes runoff in a 5′→3′ direction. We chose mRNAs with ORFs >3,000 nt to ensure that ribosome runoff was not complete within 10 min of HHT treatment and read densities could be obtained at each nucleotide position. The read densities were normalized to the average densities of the last 500 nt of the protein coding sequence (CDS) and is based on the P site of the ribosome footprints. A linear regression analysis between the HHT treatment time and ribosome runoff distances was then used to estimate a global elongation rate of 4.2 nt/s at 30°C (Figure 3C). By comparison, the global elongation rate in cultured ES calls is 1.7 nt/s at 37°C (Ingolia et al., 2011).

We performed a cluster analysis of all mRNAs with respect to number of ribosome-protected fragments (RPFs) at each time point relative to time 0. Briefly, Euclidean distance was first computed, followed by hierarchical clustering using Ward's

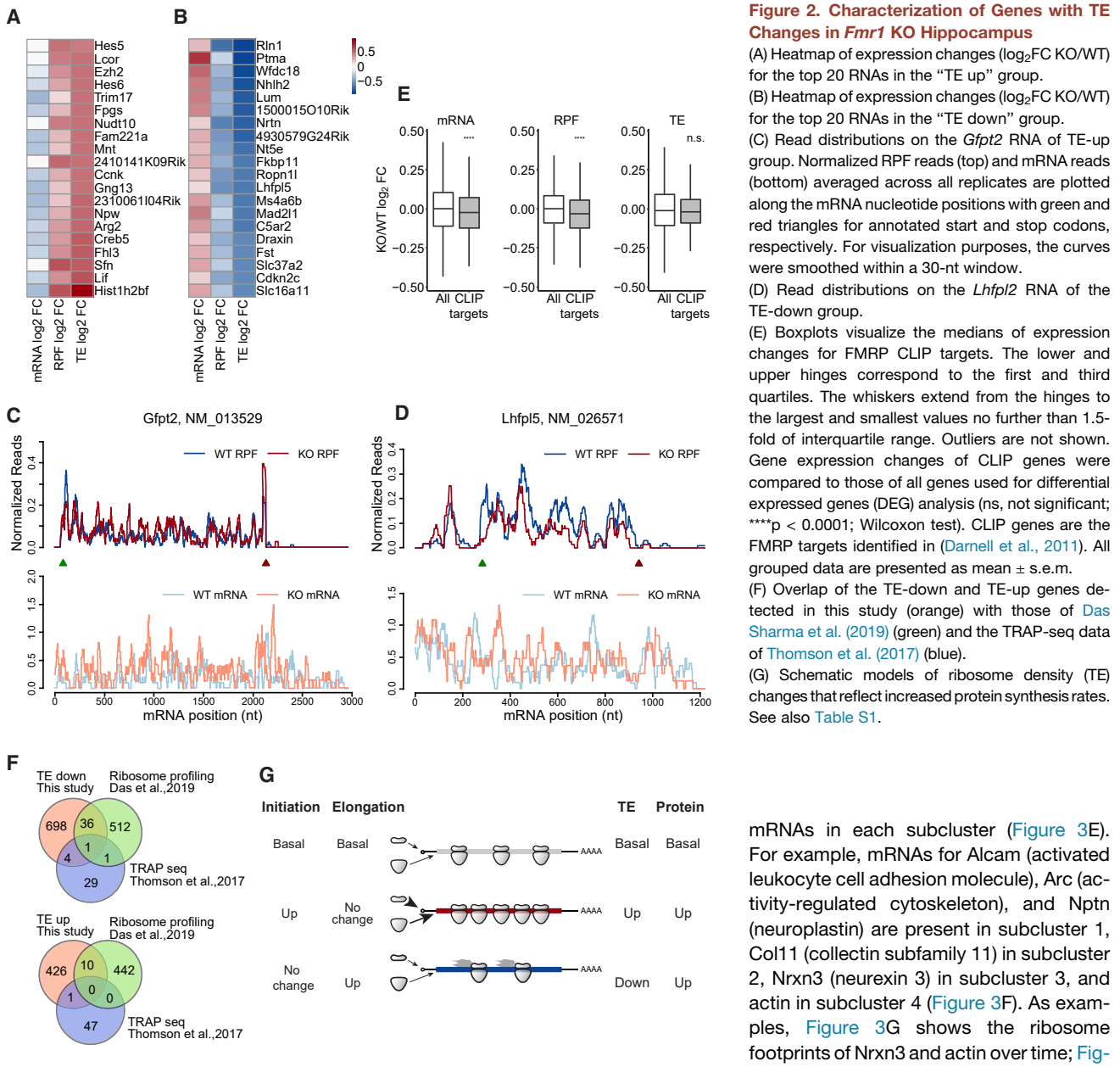

Figure 2. Characterization of Genes with TE Changes in *Fmr1* KO Hippocampus

(A) Heatmap of expression changes (log_2FC KO/WT) for the top 20 RNAs in the "TE up" group.

(B) Heatmap of expression changes (log_2FC KO/WT) for the top 20 RNAs in the "TE down" group.

(C) Read distributions on the *Gfpt2* RNA of TE-up group. Normalized RPF reads (top) and mRNA reads (bottom) averaged across all replicates are plotted along the mRNA nucleotide positions with green and red triangles for annotated start and stop codons, respectively. For visualization purposes, the curves were smoothed within a 30-nt window.

(D) Read distributions on the *Lhfpl2* RNA of the TE-down group.

(E) Boxplots visualize the medians of expression changes for FMRP CLIP targets. The lower and upper hinges correspond to the first and third quartiles. The whiskers extend from the hinges to the largest and smallest values no further than 1.5-fold of interquartile range. Outliers are not shown. Gene expression changes of CLIP genes were compared to those of all genes used for differential expressed genes (DEG) analysis (ns, not significant; ****p < 0.0001; Wilcoxon test). CLIP genes are the FMRP targets identified in (Darnell et al., 2011). All grouped data are presented as mean ± s.e.m.

(F) Overlap of the TE-down and TE-up genes detected in this study (orange) with those of Das Sharma et al. (2019) (green) and the TRAP-seq data of Thomson et al. (2017) (blue).

(G) Schematic models of ribosome density (TE) changes that reflect increased protein synthesis rates. See also Table S1.

algorithm (Ward, 1963), and the analysis of group similarities (ANOSIM) test (Clarke, 1993) was then used to assess whether distances between clusters were statistically greater than within clusters (Figure 3D). The mRNAs fell into two broad clusters (ANOSIM R = 0.56, p value < 0.001): those whose ribosome runoff occurred relatively quickly (i.e., within 5–10 min, bottom cluster), and those whose runoff occurred slowly, if at all (top cluster). These two clusters were further grouped into three subclusters each for six total subclusters (ANOSIM R = 0.64, p < 0.001). Subclusters 1–3 had slow runoff times, while subclusters 4–6 had relatively fast ribosome runoff times (Figures 3D and 3E). The ribosomes on mRNAs in subcluster 2 had the slowest runoff time. We determined the ribosome runoff patterns for the mRNAs in each subcluster (Figure 3E). For example, mRNAs for Alcam (activated leukocyte cell adhesion molecule), Arc (activity-regulated cytoskeleton), and Nptn (neuroplastin) are present in subcluster 1, Col11 (collectin subfamily 11) in subcluster 2, Nrxn3 (neurexin 3) in subcluster 3, and actin in subcluster 4 (Figure 3F). As examples, Figure 3G shows the ribosome footprints of Nrxn3 and actin over time; Figure S2A shows ribosome footprints for additional mRNAs. Although there was some CDS-length dependency of the ribosome runoff rates, the correlation was not linear (Figure S2B). GO term analysis showed that specific biological activities were associated with each subcluster. Genes in subclusters 1 and 3 (slow runoff times) were associated with neural function such as axon development and synapse organization (Figure 3H). Subcluster 2, which contained ribosomes with the slowest runoff rates, had genes encoding the extracellular matrix; subcluster 4 contained genes involved in metabolic functions; subcluster 5 was associated with mRNA processing and regulation; and subcluster 6 was associated with organelle localization (Figure S2C). These results suggest that clusters of mRNAs with specific functions have differential ribosomal transit rates.

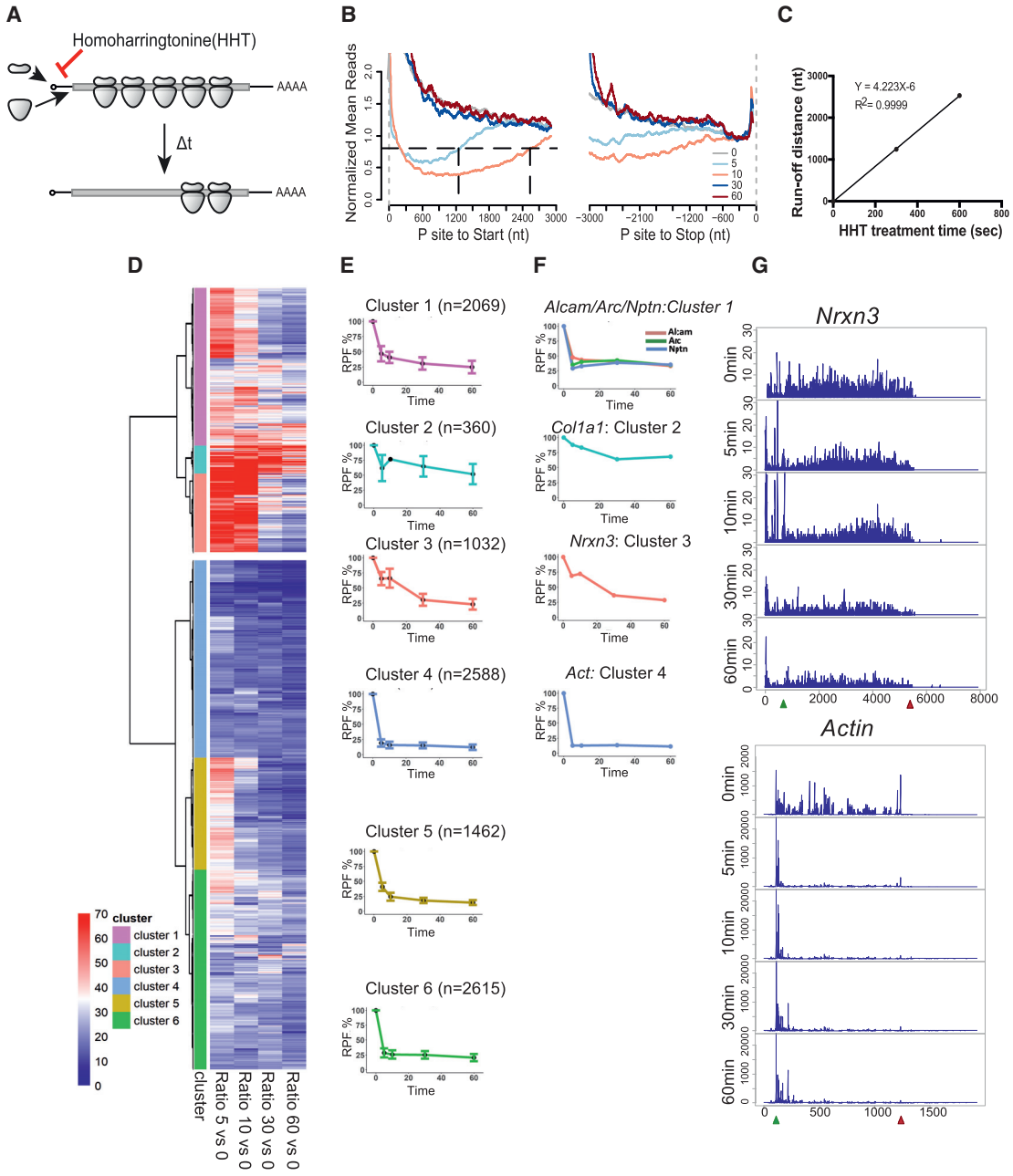

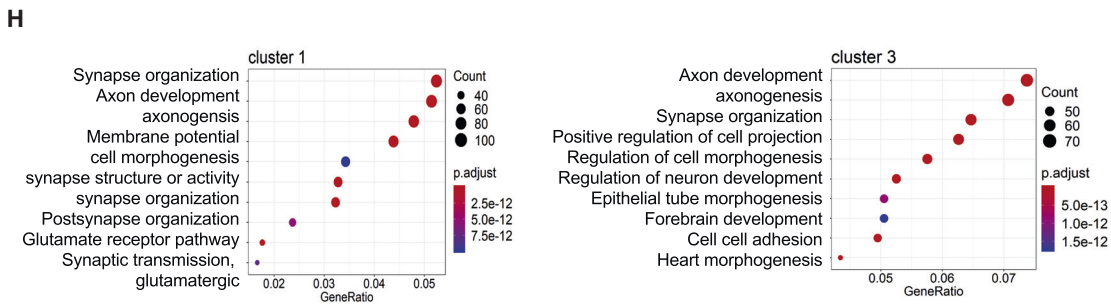

(legend on next page)

FMRP Controls Ribosome Translocation on Specific mRNAs

To investigate whether FMRP controls ribosome stalling on specific mRNAs, we first determined whether it is present in ribosome-containing complexes (Feng et al., 1997; Khandjian et al., 2004; Stefani et al., 2004; El Fatimy et al., 2016). Extracts from cortices were treated with nonionic detergent (NP40) in the presence or absence of RNase and sedimented through sucrose gradients. Figure S3A shows FMRP sedimented to a "heavy" ribosome-containing region of the gradient (Stefani et al., 2004; Darnell et al., 2011). These data suggest that FMRP is associated with ribosomes in heavy fractions and thus could play a role in ribosome stalling.

We next performed sucrose gradient analysis of slices treated with HHT for 30 min (Figure 4), which allows ribosomes on most genes to run off (cf. Figure 3). Figure 4A shows that most FMRP co-sediments with polysomes as shown previously (e.g., Feng et al., 1997; Stefani et al., 2004), but after HHT treatment, it is more prevalent in "medium" gradient fractions that correspond to four to six ribosomes most likely due to association with stalled ribosomes. Other proteins (e.g., UPF1, MAP2, and eEF2) do not show a similar change in sedimentation (Figure S3B). A small amount of FMRP remains in a heavy (>7 ribosomes) region of the gradient (Figure 4B). The same experiments were performed with *Fmr1* KO slices (Figures 4C and 4D). RNA-seq of the heavy fractions showed that 1,574 RNAs and 686 RNAs were reduced or elevated, respectively, in both genotypes, indicating a sensitivity or resistance to HHT treatment (Figure 4E). *Actin* is one RNA that was sensitive to HHT and was depleted by ribosome runoff (Figure 4F), which is consistent with results from the HHT time course (Figures 3F and 3G). *Map1b* RNA, on the other hand, was enriched in the heavy polysomes by HHT treatment (Figure 4G). Figure 4H shows GO terms for the RNAs depleted in the heavy fractions after runoff, which include factors involved in RNA metabolism. Figure 4I shows GO terms for RNAs enriched in the heavy polysomes after HHT treatment, which include factors involved in membrane and ion transport.

In contrast to the heavy polysome fractions, we found genotype-specific differences in the RNA-seq of the medium polysome fractions (Table S1). Forty-six RNAs were downregulated in HHT-treated *Fmr1* KO slices relative to WT, indicating that they are normally bound by FMRP-stalled ribosomes (Figure 5A). Eight of these mRNAs encode chromatin and transcriptional regulators, and 23 encode proteins involved in neural function (Figure 5B). One is *Ankrd12* (ankyrin repeat domain containing 12), which is depleted in the KO slices following HHT treatment (Figure 5C). Figure 5C shows that after HHT treatment, *Ankrd12* RNA contains fewer stalled ribosomes in the medium fractions of *Fmr1* KO slices, confirming this mRNA is under FMRP regulation. Figure 5D demonstrates that compared to all RNAs, the HHT-sensitive RNAs (Figure 5B) showed significant decreases in RPFs and TEs, but not RNA levels, in *Fmr1* KO relative to WT (ribosome profiling data of these RNAs from Figure 2; $^{**}p < 0.01$; $^{***}p < 0.001$, Wilcoxon test) showing the consistency between steady-state ribosome profiling and the dynamic ribosome runoff assay.

Finally, Figure 5E demonstrates that one of the mRNAs decreased in the medium fraction in the *Fmr1* KO slices, *SETD2*, shows an increase in its protein level in *Fmr1* KO hippocampus relative to WT ($p = 0.0245$, two-tailed t test), which is expected if FMRP stalls ribosome translocation on this RNA. We find no statistically significant increase in SETD2 mRNA in RNA-seq data from the FMRP KO hippocampal slices (from Figure 1). We tested SETD2 protein in immortalized mouse embryonic fibroblasts (MEFs) derived from WT and *Fmr1* KO mice and found no change relative to genotype (Figure S5E). This result might reflect a possible brain-specific function of FMRP or that rapidly dividing MEF cell lines do not recapitulate FMRP-dependent ribosome stalling, at least not on SETD2 mRNA. SETD2 is the main histone lysine methyltransferase that trimethylates the histone H3 tail on the lysine36(K36).

FMRP-Mediated Regulation of H3K36me3

To investigate whether altered SETD2 levels influence gene-specific changes in H3K36me3, we performed ChIP-seq from WT and *Fmr1* KO hippocampus in duplicate, combining hippocampal tissue from two animals per biologic replicate (Figure 6A). All genotypic replicates were highly correlated with each other (Figure S4A). H3K36me3 is a broad histone mark that is enriched primarily in the body of the gene. To measure regions with enrichment of the mark, we used the SICER v1.1 package (Xu et al., 2014) that annotates ChIP signal over a stretch of DNA as "islands" (an island is defined as a cluster of non-overlapping consecutive DNA regions (200-bp windows) separated by at least a 600-bp gap region of DNA with no

Figure 3. Runoff Ribosome Profiling of WT Mouse Brain Slices

(A) Schematic diagram of homoharringtonine (HHT) runoff ribosome profiling. WT mouse brain slices were treated with 20 μM HHT, an inhibitor of translation initiation, to allow ribosome runoff for 5, 10, 30, and 60 min (t) at 30°C. 10 slices from two or three mice were pooled per time point of HHT treatment.

(B) Metagene plot of RPFs after HHT treatment. Reads are mapped transcripts (n = 1,401) with CDS longer than 3,000 nt and aligned at the annotated start and stop codons (gray vertical dash lines). The read densities at each nucleotide position are normalized to the average density of the last 500 nt of CDS and averaged using the P sites of RPFs. For visualization purposes, the curves were smoothed within a 90-nt window. Black horizontal dash line indicates the arbitrary 0.8 threshold to estimate the relative runoff distances (black vertical dash lines).

(C) Linear regression between the HHT treatment time and ribosome run-off distances (from B) to estimate the global elongation rate (4.2 nt/s).

(D) Cluster analysis of gene groups with distinct ribosome runoff patterns. The RPFs of each gene at each time point was normalized to time 0. The Euclidean distance matrix was then calculated, followed by hierarchical clustering using Ward's agglomeration method (Ward, 1963).

(E) Ribosome runoff patterns for each subcluster. The global pattern of each subcluster was summarized using the corresponding median and standard deviation in each time point. The number of RNAs in each subcluster is shown in parentheses.

(F) Representative ribosome runoff profiles that reflect each subcluster. The runoff pattern for *Actin* is similar to subclusters 4–6.

(G) Ribosome footprints for *Nrxn3* and *Actin* mRNAs during the runoff time period.

(H) GO terms for subclusters 1 and 3. Gene ratio refers to the percentage of total differentially expressed genes in the given GO term.

See also Figure S2 and Table S1.

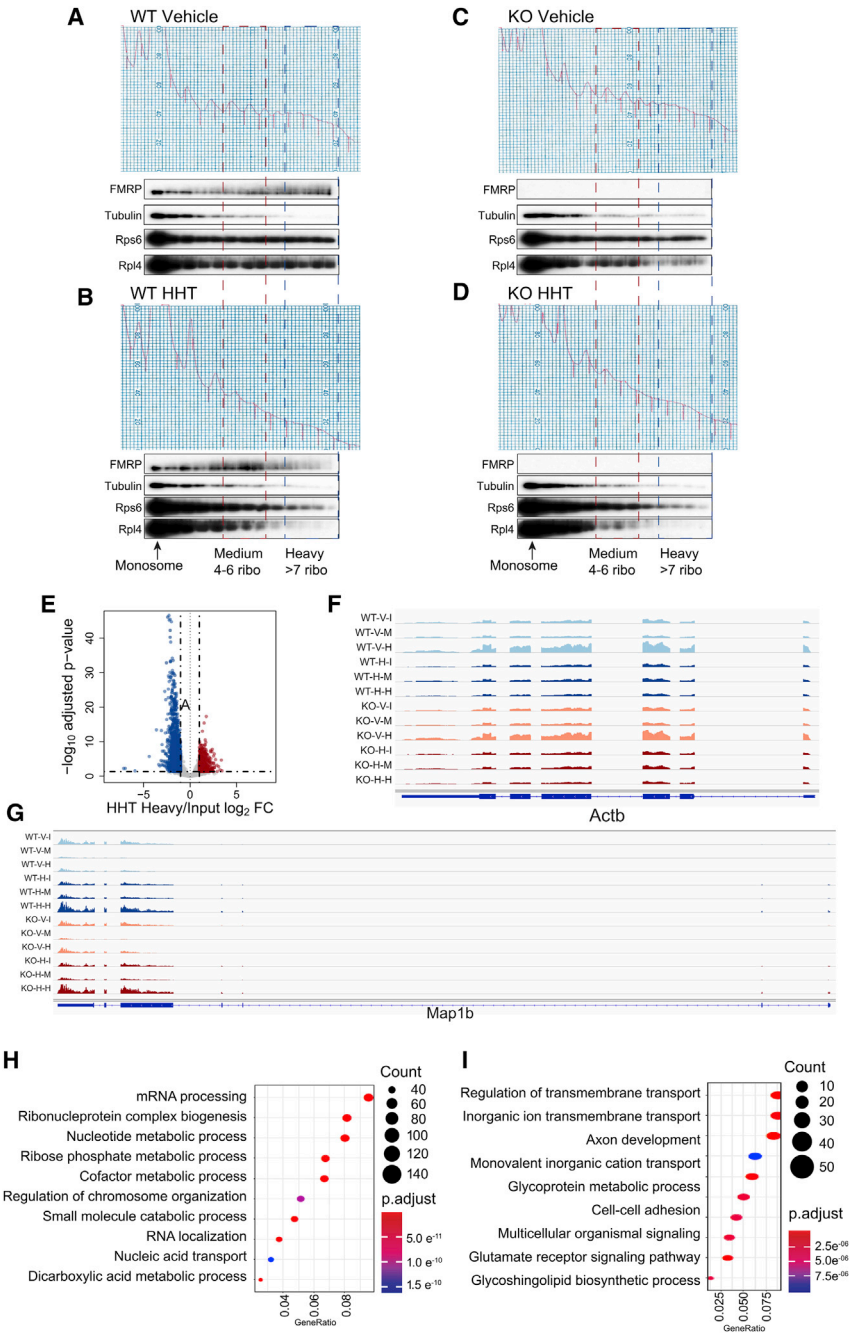

Figure 4. Substantial FMRP Remains Associated with Polysomes after HHT Treatment

(A–D) WT mouse hippocampal slices were treated with DMSO vehicle (A) or 20 μM HHT (B) for 30 min at 30°C. In parallel, *Fmr1* KO mouse hippocampal slices were also treated with DMSO vehicle (C) or 20 μM HHT (D) for 30 min at 30°C. Slices were homogenized and applied to 15%–45% (w/w) sucrose gradients, which were fractionated with continuous monitoring of A_{260} after ultracentrifugation. Fractions were collected for immunoblotting with indicated antibodies to detect the association of FMRP with polysomes. 10 slices from two or three mice/genotype were pooled per biological replicate (WT, n = 2; *Fmr1* KO, n = 2).

(E) RNA sedimenting to heavy fractions containing more than seven ribosomes from WT slices treated with HHT was analyzed relative to input. 1,574 RNAs were reduced and 686 were elevated relative to input after HHT treatment.

(F) *Actin* mRNA reads in the designated conditions (WT; V, vehicle, I, input; H, heavy fractions; KO, *Fmr1* KO).

(G) *Map 1b* mRNA reads in the designated conditions.

(H) GO terms of RNAs depleted in heavy fractions relative to WT.

(I) GO terms of RNAs enriched in heavy fractions relative to WT.

See also Figure S3 and Table S1.

ChIP-enriched signal detected above threshold). Annotation of the H3K36me3 islands shows that they were primarily present within the gene body compared to promoter proximal regions, as expected (Krogan et al., 2003; Tiedemann et al., 2016) (Figure 6B). Metagene analysis showed there to be no genotype-specific difference in the distribution of marks overall along the gene body and no effect of gene length (Figures S4B–S4D). We further compared the differential enrichment of the H3K36me3 islands within the replicates by a negative binomial test performed using edgeR (Robinson et al., 2010) (fold change >2 and $p < 0.05$). We found 363 islands with decreased and 2,223 islands with increased H3K36me3 in the *Fmr1* KO compared to WT hippocampus ChIP-seq in both replicates (Table S2). Examples of the changes of these marks that are genotype-dependent are shown in Figure 6C where H3K36me3 on *Reep4* (receptor expression-enhancing protein 4) is reduced but elevated on *Tprkb* (TP53-related protein kinase-binding protein). The decreased islands were fewer and mostly found in intragenic regions, whereas the increased islands were enriched and present in both the intragenic and intergenic regions (Figure 6D), demonstrating a redistribution of H3K36me3 in FXS model mice. Many of the islands, especially those that increase in *Fmr1* KO animals, are found on genes linked to autism spectrum disorders as defined by Simons Foundation Autism Research Initiative (SFARI) (Figure 6E). A subset of genes (37) showed both increased and decreased islands, but at different locations on the gene body (Figure 6E). GO term enrichment analysis of the genes that increased H3K36me3 islands is shown in Figure 6F. The genes with increased H3K36me3 islands are remarkably enriched for those involved in neural function such as synapse assembly and animal behavior. No significant GO terms were enriched in the group of genes with decreased H3K36me3 islands. We find no correlation between steady-state RNA abundance and

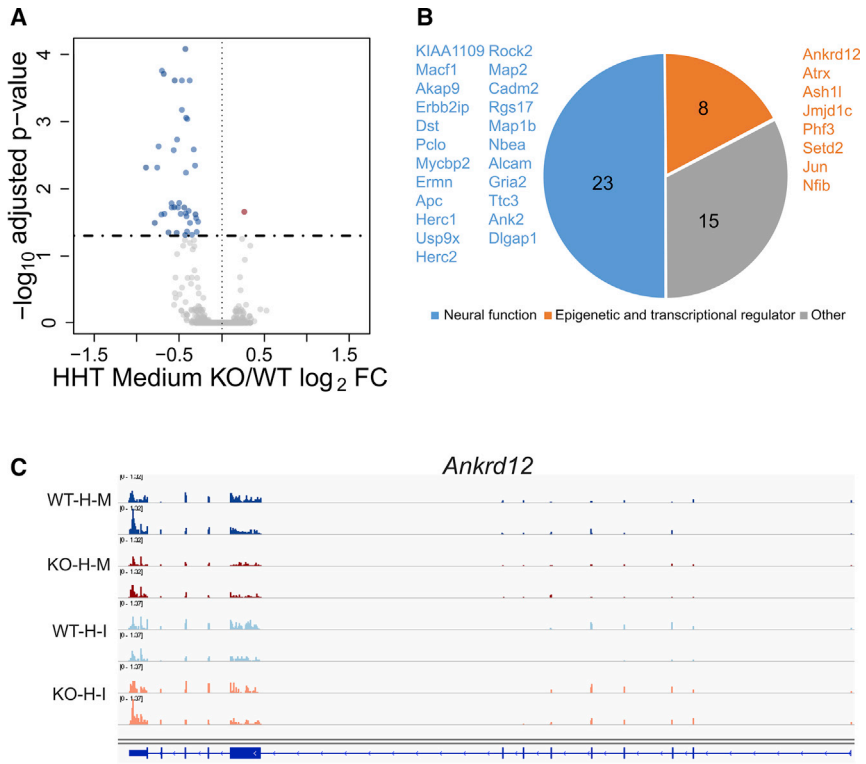

Figure 5. FMRP Stalls Ribosomes on Specific mRNAs

(A) RNA sedimenting to medium polysomes containing four to six ribosomes after HHT treatment of hippocampal slices; 46 RNAs are downregulated and 1 is upregulated in *Fmr1* KO relative to WT.

(B) Downregulated RNAs in HHT-treated *Fmr1* KO slices primarily encode epigenetic and transcriptional regulators and proteins involved in neural function.

(C) Example of *Ankrd12* RNA, which has reduced reads in *Fmr1* KO slices relative to WT after HHT (H) treatment. Input (I) reads are similar in both genotypes. M refers to medium fraction.

(D) Boxplot showing the fold change of *Fmr1* KO versus WT of all RNAs (white) compared to those identified in (A) and (B) (gray) with respect to steady-state RNA levels, RPFs, and TE (ns, not significant; $^{**}p < 0.01$; $^{***}p < 0.001$; Wilcoxon test). All grouped data are presented as mean ± s.e.m.

(E) Western blot analysis of SETD2 and lamin AC in hippocampus from four WT and five *Fmr1* KO mice. When quantified and made relative to lamin AC, SETD2 was significantly increased in the KO ($p = 0.0245$, two-tailed t test). All grouped data are presented as mean ± s.e.m.

See also Table S1 and Figure S5E.

H3K36me3 levels on islands in the genes (Figure S4F), which could be attributed to compensatory post-transcriptional mechanisms affecting steady-state RNA. Furthermore, the methylated islands also undergo genotype-specific length changes; they are significantly longer in the WT compared to *Fmr1* KO ($p < 0.001$, Kolmogorov-Smirnov [K-S] test) (Figure S4E). Our data thus show that an increase in the levels of SETD2 in the *Fmr1* KO resulting primarily in increased H3K36me3 chromatin marks at a subset of genes.

FMRP Regulates Alternative RNA Processing

H3K36me3 in mammals has been correlated with alternative pre-mRNA splicing (Kim et al., 2011). We analyzed our RNA-seq data from WT and *Fmr1* KO hippocampal slices using the rMATS alternative splicing package (Shen et al., 2014) and detected many alternative pre-mRNA processing events including skipped exon (SE), mutually excluded exon (MXE), and alternative 5′ and 3′ splice site (A5SS and A3SS) (Figure 7A; Table S3; FDR < 5% and $p < 0.05$). The number of exon inclusion events are shown (differences in exon inclusion levels is calculated as percent spliced in [PSI], and a cutoff of |deltaPSI| ≥5% is used). Several of the exon-skipping events were validated by qRT-PCR, with ~20%–40% reduction in exon skipping in the *Fmr1* KO relative to WT (Figure 7B). These skipped exons have previously been found to be associated with defects in brain development and disease pathology (An and Grabowski, 2007; Fugier et al., 2011; Rockenstein et al., 1995; Wang et al., 2018). In particular, an increase in microexon 4 skipping in *Cpeb4* mRNA was found in postmortem cortical tissue from autism patients. Consequently, a mouse model of *Cpeb4* microexon 4 deletion recapitulated the molecular and behavioral phenotypes found in autism patients (Irimia et al., 2014; Parras et al., 2018; Quesnel-Vallières et al., 2016). Figure 7C shows all the RNA processing events that undergo changes in *Fmr1*-deficient hippocampus relative to WT ($p < 0.05$, |deltaPSI| ≥5%). Skipped exons are by far the most prevalent category, followed by alternative 3′ splice sites. The genes whose RNA processing events are altered in *Fmr1* KO are strongly linked to neural function such as vesicle transport to synapses and vesicle recycling (Figure 7D). Moreover, many of the genes with alternative splicing events (Alt. Spl.) in *Fmr1* KO hippocampus (Alt. Spl. *Fmr1* KO) are linked to autism (i.e., SFARI autism spectrum disorder database [ASD]) (Figure 7E). In addition, the Alt. Spl. genes in *Fmr1* KO significantly overlap with genes previously found to display alternative splicing in patients with autism (Alt. Spl. ASD) (Parikshak et al., 2016) (Figure 7E). We also find an overlap of genes with changes in H3K36me3 islands with those

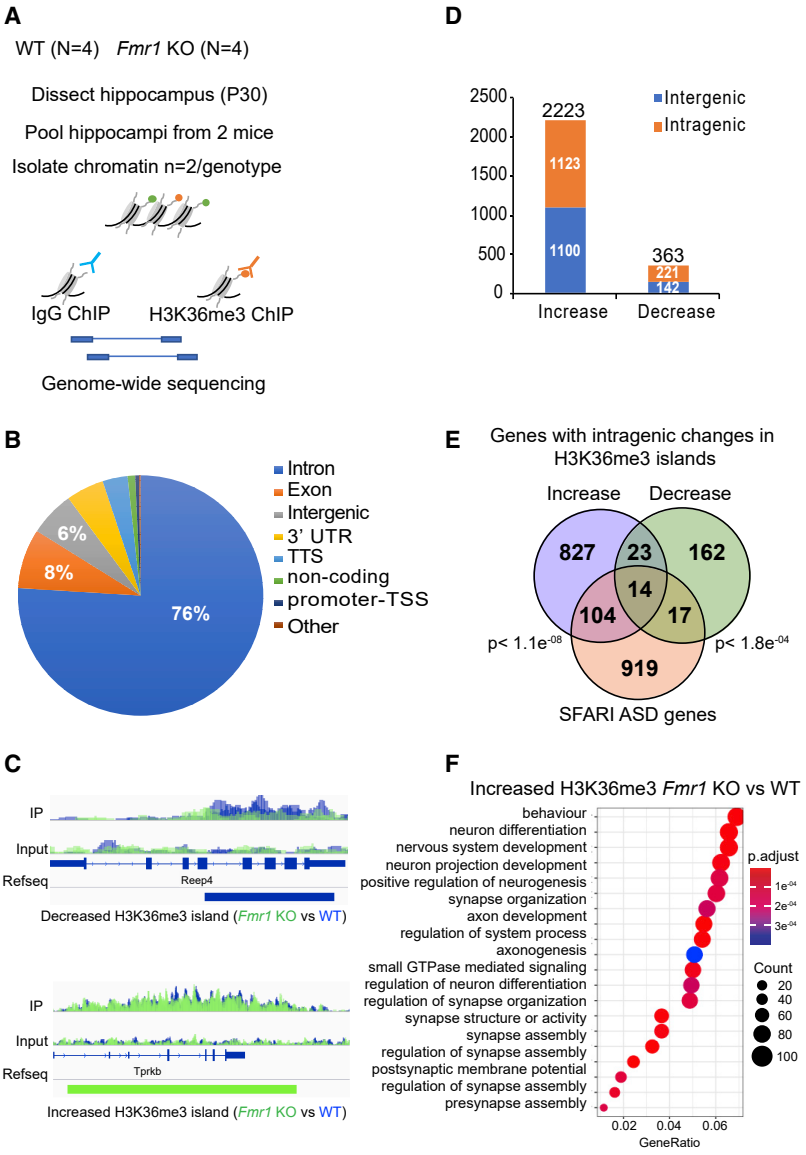

Figure 6. H3K36me3 Localization Is Altered in *Fmr1* KO Hippocampus

(A) Experimental design for *in vivo* ChIP-seq of H3K36me3 in hippocampus from adult WT (n = 4) and *Fmr1* KO (n = 4) mice.

(B) Pie chart representing the genomic annotation of the total H3K36me3 islands identified in the WT and *Fmr1* KO ChIP-seq.

(C) H3K36me3 ChIP-seq gene tracks for WT and *Fmr1* KO hippocampal tissue. The two sequencing tracks from each biological replicate (n = 2 [pooled hippocampi from two mice/biological replicate]) of WT and *Fmr1* KO were merged and overlaid. WT ChIP-seq tracks are in blue, and KO tracks are in green. The tracks for immunoprecipitation (IP) and input are displayed. The islands with significantly decreased (blue) or increased (green) tracks are shown below the RefSeq gene annotation (FDR < 0.0001; $p < 0.01$) as identified using the SICER package. *Reep4* shows decreased H3K36me3 islands in *Fmr1* KO, and *Tprkb* shows increased islands in *Fmr1* KO.

(D) Distribution of significantly increased or decreased H3K36me3 islands in intragenic and intergenic regions of the genome using negative binomial test performed using edgeR (Robinson et al., 2010) (fold change >2 and $p < 0.05$). The total number of increased or decreased islands is indicated above the respective bars in the graph in *Fmr1* KO versus WT ChIP-seq.

(E) Venn diagram for significant overlap of *Fmr1* KO mis-regulated H3K36me3 genes (increased islands in blue and decreased islands in green) with the ASD-linked genes from the SFARI database. A subset of genes showed both increased and decreased islands along the length of the gene body. The p value (hypergeometric test) is indicated next to the respective comparisons.

(F) GO term enrichment of H3K36me3 differentially enriched genes in *Fmr1* KO versus WT (p adjust value < 0.05). Gene ratio refers to the percentage of total differentially expressed genes in the given GO term.

See also Figure S4 and Table S2.

found to harbor aberrant splicing in *Fmr1* KO tissue (Figure 7E). We found no correlation between amount of exon skipping and RNA abundance, RPF levels or presence of FMRP CLIP tags at the gene level (Figures S5A–S5C). We next assessed the H3K36me3 levels at the skipped exons in the SE category and found a significant decrease in the H3K36me3 marks at the 5′ splice site (±50 nt) of these exons that are skipped in the *Fmr1* KO hippocampus compared to the WT (Figure 7F; p = 0.02 using the Wilcoxon test). Interestingly, when we increased the analysis over a region of ± 150 nt (~2 nucleosomes) we no longer found a decrease in H3K36me3 at the skipped exons in the FMRP KO animal (Figure S5D). Although at the island level, which encompasses mainly regions >1 kb, we see mainly an increase in H3K36me3 levels, but at the 5′ splice site of genes (±50 nt) susceptible to alternative splicing in the FMRP KO, we see a decrease in H3K36me3 levels. Further studies are needed to understand how H3K36me3 modifications and/or other factors might play a role in regulating differential alternative splicing in the FMRP KO background. Thus, as with other autism spectrum disorders, dysregulated alternative splicing is prevalent in a mouse model of FXS and might be linked to changes in H3K36me3 levels at the splice site.

DISCUSSION

We used several approaches to investigate FMRP regulation of mRNA expression in the mouse brain, focusing first on steady-state ribosome profiling in hippocampal slices. *Fmr1* deficiency resulted in ribosome footprint levels that mostly tracked altered levels of RNA, which is consistent with other studies (Liu et al., 2018, 2019; Das Sharma et al., 2019). Because ribosome profiling at steady state cannot distinguish between static and translocating ribosomes, we modified our profiling procedure (Ingolia et al., 2011) to identify the dynamic range of ribosome translocation rates genome-wide in hippocampal slices. These studies in turn resulted in four main findings. First, they showed

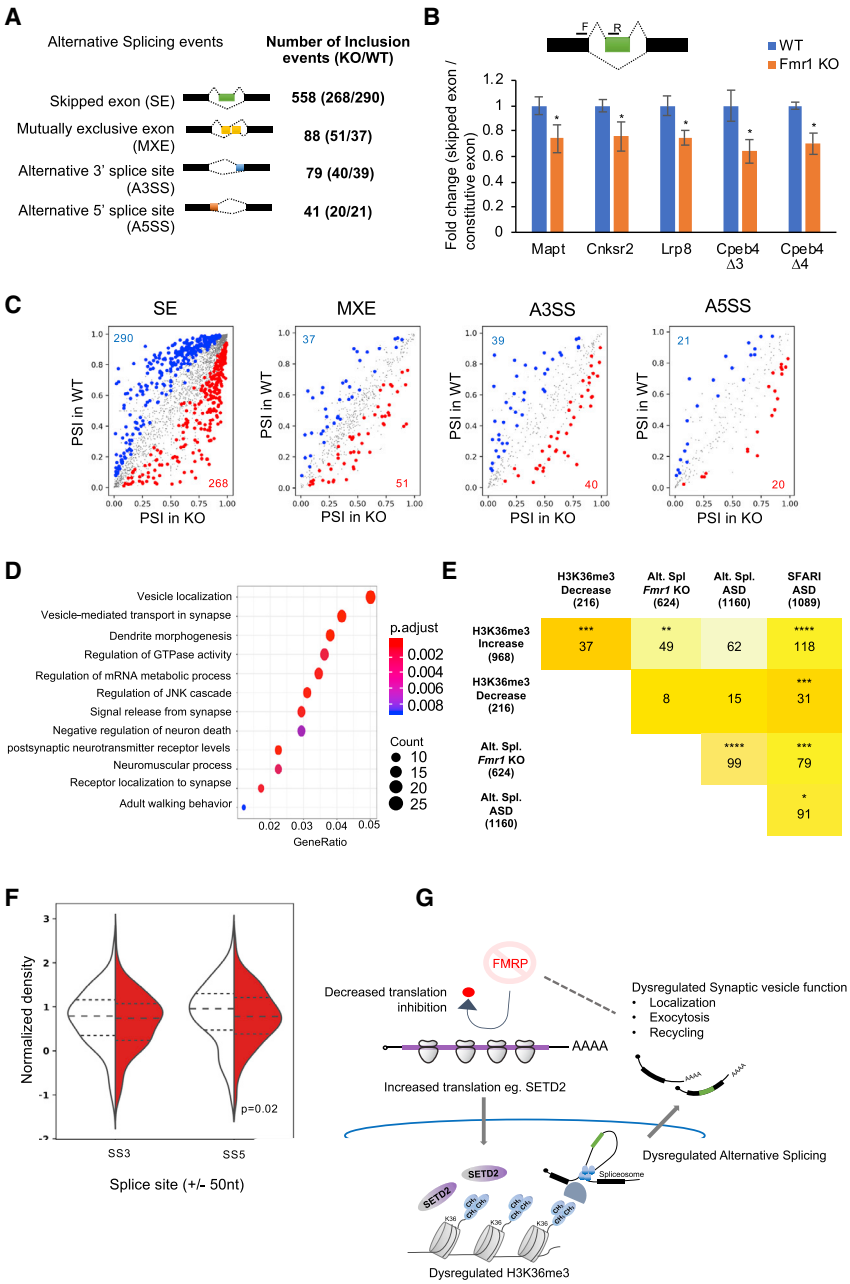

Figure 7. Global Analysis of FMRP-Mediated Alternative Splicing

(A) Summary table of total splicing events in *Fmr1* KO and WT based on RNA-seq from hippocampal slices. Splicing events detected by rMATS at a FDR <5% and a difference in the exon inclusion levels between the genotypes (deltaPSI) ≥5% are depicted.

(B) Alternative splicing events validated using qRT-PCR are shown for several RNAs (hippocampus tissue, WT, n = 6; *Fmr1* KO, n = 6). The illustration depicts an example of exon skipping (green box) in the *Fmr1* KO. Primer positions are depicted with black bars. All grouped data are presented as mean ± s.e.m.

(C) Alternative splicing events detected in *Fmr1* KO and WT hippocampus. Inclusion events that were significantly ($p < 0.05$) increased (red), decreased (blue), or unchanged (gray) are indicated. The numbers of events in the up or down category are shown in red and blue, respectively. PSI, percent splice in/exon inclusion levels.

(D) GO term enrichment for all alternative splicing events are shown (p adjust value < 0.05). The total number of genes identified in the RNA-seq from (Figure 1) was used as background. Gene ratio refers to the percentage of total differentially expressed genes in the given GO term.

(E) Table depicting the overlap of the alternative splicing events (Alt. Spl.) in genes in this study with the SFARI autism spectrum disorder database, the Alt. Spl. genes identified in samples from autism patients (Parikshak et al., 2016), and genes with increased or decreased H3K36me3 islands from Figure 6. The intensity of the color represents the increasing number of overlapping genes between the gene sets. Asterisks indicate statistical significance (*$p < 0.05$; ***$p < 0.001$; ****$p < 0.0001$, hypergeometric test).

(F) Violin plot for the H3K36me3 ChIP signal at ±50 nt of the 5′ (SS5) and 3′ (SS3) splice sites of the alternatively skipped exons in WT (white) and *Fmr1* KO (red) hippocampus tissue ($p < 0.05$, K-S test for significance). See also Figures S5E and S5F.

(G) Model for FMRP-mediated alterations in H3K36me3 marks on the chromatin and alternative splicing of transcripts in the hippocampus.

See also Table S3.

that mRNAs cluster into defined functional biology groups based on the transit rates of their associated ribosomes. The ribosomes on most mRNAs (>5,000) transit rapidly, whereas on some mRNAs (~3,000), ribosome transit is slow or nearly not at all (~350). There is some CDS length dependency as well. Second, using a combination of ribosome runoff and sucrose gradient centrifugation, we identified ~50 mRNAs associated with FMRP-stalled ribosomes, which strongly imply translational regulation. One of these mRNAs encodes a histone lysine methyltransferase, SETD2, which is elevated in *Fmr1* KO hippocampus. Third, the SETD2-dependent histone mark, H3K36me3, is rearranged in both intragenic and intergenic regions upon *Fmr1* deficiency; primarily increases in H3K36me3 are observed in *Fmr1* KO. Fourth, because H3K36me3 has been correlated with alternative RNA processing in mammals (Kim et al., 2011), we analyzed our RNA-seq data and found widespread aberrant splicing in the *Fmr1* KO hippocampus, most prominently exon skipping/inclusion. These altered processing events often correlated with changes in the histone mark, occurred on genes that regulate pre-synaptic functions, such as synaptic vesicle recycling, and were strongly linked to autism spectrum disorders (Figure 7E).

Earlier studies have inferred that ribosome stalling in the brain is linked to RNA transport granules in dendrites (Krichevsky and

Kosik 2001; Mallardo et al., 2003; Kanai et al., 2004; Khandjian et al., 2004; Graber et al., 2013). It is possible that at least some of the ribosome stalling we observe may be the result from such compartmentalization in neurons or perhaps is a more general feature of the brain. In contrast, rapidly dividing ES cells do not appear to have stalled ribosomes, at least not of the magnitude we observe here (Ingolia et al., 2011). Irrespective of whether ribosome stalling is a dendritic or neuronal phenomenon, how it occurs mechanistically on specific mRNAs is unclear, but it could be related to secondary structure or association with RNA binding or other proteins. One clue, however, could be the accumulating evidence that strongly implicates phosphorylation of eEF2 as a coordinator of translation and neural activity and thus is likely to be one mediator of ribosome translocation rates (Scheetz et al., 2000; Sutton et al., 2007; Park et al., 2008; McCamphill et al., 2015; Heise et al., 2017). Even so, the involvement of phospho-eEF2, a general translation factor, would unlikely be responsible for mRNA-specific stalling. We also noted that some mRNAs, such as those in subcluster 2 (Figures 3D and 3E), encode proteins involved in the extracellular matrix (Figure S2C). A number of these proteins contain proline-rich stretches, whose geometry in the polypeptide exit tunnel can lead to ribosome stalling (Schuller et al., 2017; Huter et al., 2017).

We have identified 48 mRNAs whose ribosomes are stalled specifically by FMRP. These RNAs include those with (40 mRNAs) and without FMRP CLIP (8 mRNAs) sites in coding regions (Darnell et al., 2011; Van Driesche et al., 2019), so it would appear that a simple FMRP "roadblock" model would not explain ribosome stalling. Alternatively, Ishizuka et al. (2002) showed that *Drosophila* FMRP binds ribosomal proteins, and in a cryoelectron microscopy (cryo-EM) study, Chen et al. (2014) found that *Drosophila* FMRP reconstituted with mammalian ribosomes binds a region that would preclude tRNA and elongation factors from engaging in translation. However attractive this model is for FMRP-mediated ribosome stalling, the fact that mRNA or translation factors were not included in the reconstitution assays brings into question whether it reflects the physiological basis for ribosome stalling.

Our studies revealed that FMRP stalls ribosomes on a number of mRNAs that encode epigenetic regulators and that the misregulation of one of them in *Fmr1*-deficient hippocampus, SETD2, leads to a widespread increase in H3K36me3 chromatin marks (islands). These H3K36me3 islands are both enriched for and depleted from autism-risk genes (Figure 6E) as well as those with synaptic functions (Figure 6F). This suggests that SETD2, the main enzyme that catalyzes this chromatin mark, might also be an autism-risk gene, which has been previously reported (Lumish et al., 2015). Mutations in several chromatin-remodeling genes have been linked to changes in neural function, autism, and other intellectual disabilities (van Bokhoven 2011; Goodman and Azad, 2019). In most cases, however, mutations in epigenetic modifiers result in up or downregulation of transcription. Indeed, previously identified epigenetic changes in FXS model mice by Korb et al. (2017), particularly H3K4me3, H4K8ac, and H4K16ac, were responsible for widespread changes in transcription in cortical neurons and the cerebellum. Importantly, these investigators could rescue several FXS pathophysiologies, many of which resemble those in autism, by targeting the epigenetic reader protein Brd4. H3K36me3 does not mark promoter regions but instead is found in gene bodies and increases as RNA polymerase II proceeds 3′ during catalysis (Neri et al., 2017). In mammals, one of the functions H3K36me3 is correlated with, if not causative for, is alternative pre-mRNA processing (Kim et al., 2011). In the *Fmr1*-deficient hippocampus, we detected extensive changes in RNA processing, mostly exon skipping. Surprisingly, most of the skipped exons occurred in genes that have pre-synaptic functions such as synaptic vesicle recycling, transport, and exocytosis, which could at least partially explain alterations in synaptic vesicle dynamics and neurotransmitter release in FXS model mice (Deng et al., 2013; Ferron et al., 2014; Broek et al., 2016). Furthermore, a number of skipped exons in *Fmr1* KO have been linked to neurological disorders such as autism (skipped microexon 4 in *Cpeb4*; Irimia et al., 2014; Parras et al., 2018; Quesnel-Vallières et al., 2016), Alzheimer's disease (skipped exon 7 in *APP*; Fragkouli et al., 2017; Rockenstein et al., 1995), Parkinson's disease (skipped exon 3 in *Mapt*; Lai et al., 2017; Wobst et al., 2017), and intellectual disabilities (skipped exon 12 in *Cnksr2*; Houge et al., 2012).

Alternative pre-mRNA processing is a common feature in autism (Raj and Blencowe, 2015; Quesnel-Vallières et al., 2019), so it is perhaps not surprising that this would occur in fragile X. However, because FMRP is an RNA-binding protein that regulates translation, a reasonable assumption would be that mRNAs encoding splicing factors are improperly expressed in the disorder and that this leads directly to mis-splicing events. However, our data indicate that this relationship might not be linear. Instead, we find that FMRP controls ribosome dynamics on specific mRNAs, which leads to elevated translation (e.g., SETD2), which leads to chromatin modifications (e.g., H3K36me3), which in turn might lead to alternative splicing of neuronal mRNAs (Figure 7G). These observations do not preclude the possible, if not likely, direct involvement of FMRP in some of these events. Even so, inferences that fragile X is a disorder of improper translation, while not incorrect, are vastly oversimplified. However, the complexity of gene expression changes in fragile X might offer opportunities for therapeutic intervention at multiple steps.

STAR★METHODS

Detailed methods are provided in the online version of this paper and include the following:

- KEY RESOURCES TABLE
- LEAD CONTACT AND MATERIALS AVAILABILITY
- EXPERIMENTAL MODEL AND SUBJECT DETAILS
  - Cell culture
- METHOD DETAILS
  - Mouse acute brain slice preparation
  - Sucrose gradients of hippocampal slices for steady-state ribosome profiling
  - Sucrose gradients of cortical-hippocampal slices for run-off ribosome profiling
  - Sucrose gradients of cortical-hippocampal slices for polysome profiling

SUPPLEMENTAL INFORMATION

Supplemental Information can be found online at https://doi.org/10.1016/j.celrep.2020.02.076.

ACKNOWLEDGMENTS

We thank Lori Lorenz, Craig Peterson, Huan Shu, and Danesh Moazed for valuable discussions. J.D.R., K.M.H., B.L., and S.S. conceived various aspects of the project. We thank Maria Ivshina and Suna Jung for providing reagents. This work was supported by grants from the National Institutes of Health (NIH) (grants U54HD82013 to J.D.R. and U54HD082008 to K.M.H.), the Simons Foundation for Autism Research Initiative (grant 400998 to J.D.R. and K.M.H.), and the Charles H. Hood Foundation (to J.D.R.). S.S. was supported by a postdoctoral fellowship from the FRAXA Foundation.

AUTHOR CONTRIBUTIONS

B.L., G.M., and S.S. performed the experiments. R.W. provided essential help with bioinformatics. J.D.R. wrote the manuscript with input from all authors.

DECLARATION OF INTERESTS

The authors declare no competing interests.

Received: October 7, 2019
Revised: December 24, 2019
Accepted: February 19, 2020
Published: March 17, 2020

REFERENCES

An, P., and Grabowski, P.J. (2007). Exon silencing by UAGG motifs in response to neuronal excitation. PLoS Biol. *5*, e36.

Anderson, B.R., Chopra, P., Suhl, J.A., Warren, S.T., and Bassell, G.J. (2016). Identification of consensus binding sites clarifies FMRP binding determinants. Nucleic Acids Res. *44*, 6649–6659.

Ascano, M., Jr., Mukherjee, N., Bandaru, P., Miller, J.B., Nusbaum, J.D., Corcoran, D.L., Langlois, C., Munschauer, M., Dewell, S., Hafner, M., et al. (2012). FMRP targets distinct mRNA sequence elements to regulate protein expression. Nature *492*, 382–386.

Bowling, H., Bhattacharya, A., Zhang, G., Alam, D., Lebowitz, J.Z., Bohm-Levine, N., Lin, D., Singha, P., Mamcarz, M., Puckett, R., et al. (2019). Altered steady state and activity-dependent de novo protein expression in fragile X syndrome. Nat. Commun. *10*, 1710.

Brar, G.A., and Weissman, J.S. (2015). Ribosome profiling reveals the what, when, where and how of protein synthesis. Nat. Rev. Mol. Cell Biol. *16*, 651–664.

Broek, J.A.C., Lin, Z., de Gruiter, H.M., van 't Spijker, H., Haasdijk, E.D., Cox, D., Ozcan, S., van Cappellen, G.W.A., Houtsmuller, A.B., Willemsen, R., et al. (2016). Synaptic vesicle dynamic changes in a model of fragile X. Mol. Autism *7*, 17.

Chen, E., Sharma, M.R., Shi, X., Agrawal, R.K., and Joseph, S. (2014). Fragile X mental retardation protein regulates translation by binding directly to the ribosome. Mol. Cell *54*, 407–417.

Clarke, K.R. (1993). Non-parametric multivariate analyses of changes in community structure. Aust. J. Ecol. *18*, 117–143.

Cotney, J.L., and Noonan, J.P. (2015). Chromatin immunoprecipitation with fixed animal tissues and preparation for high-throughput sequencing. Cold Spring Harb. Protoc. *2015*, 191–199.

Darnell, J.C., Van Driesche, S.J., Zhang, C., Hung, K.Y., Mele, A., Fraser, C.E., Stone, E.F., Chen, C., Fak, J.J., Chi, S.W., et al. (2011). FMRP stalls ribosomal translocation on mRNAs linked to synaptic function and autism. Cell *146*, 247–261.

Das Sharma, S., Metz, J.B., Li, H., Hobson, B.D., Hornstein, N., Sulzer, D., Tang, G., and Sims, P.A. (2019). Widespread alterations in translation elongation in the brain of juvenile Fmr1 knockout mice. Cell Rep. *26*, 3313–3322.e5.

Deng, P.Y., Rotman, Z., Blundon, J.A., Cho, Y., Cui, J., Cavalli, V., Zakharenko, S.S., and Klyachko, V.A. (2013). FMRP regulates neurotransmitter release and synaptic information transmission by modulating action potential duration via BK channels. Neuron *77*, 696–711.

Dixon, P. (2003). VEGAN, a package of R functions for community ecology. J. Veg. Sci. *14*, 927–930.

Dölen, G., Osterweil, E., Rao, B.S., Smith, G.B., Auerbach, B.D., Chattarji, S., and Bear, M.F. (2007). Correction of fragile X syndrome in mice. Neuron *56*, 955–962.

El Fatimy, R., Davidovic, L., Tremblay, S., Jaglin, X., Dury, A., Robert, C., De Koninck, P., and Khandjian, E.W. (2016). Tracking the fragile X mental retardation protein in a highly ordered neuronal ribonucleoparticles population: a link between stalled polyribosomes and RNA granules. PLoS Genet. *12*, e1006192.

Feng, Y., Absher, D., Eberhart, D.E., Brown, V., Malter, H.E., and Warren, S.T. (1997). FMRP associates with polyribosomes as an mRNP, and the I304N mutation of severe fragile X syndrome abolishes this association. Mol. Cell *1*, 109–118.

Ferron, L., Nieto-Rostro, M., Cassidy, J.S., and Dolphin, A.C. (2014). Fragile X mental retardation protein controls synaptic vesicle exocytosis by modulating N-type calcium channel density. Nat. Commun. *5*, 3628.

Fragkouli, A., Koukouraki, P., Vlachos, I.S., Paraskevopoulou, M.D., Hatzigeorgiou, A.G., and Doxakis, E. (2017). Neuronal ELAVL proteins utilize AUF-1 as a co-partner to induce neuron-specific alternative splicing of APP. Sci. Rep. *7*, 44507.

Fugier, C., Klein, A.F., Hammer, C., Vassilopoulos, S., Ivarsson, Y., Toussaint, A., Tosch, V., Vignaud, A., Ferry, A., Messaddeq, N., et al. (2011). Misregulated alternative splicing of BIN1 is associated with T tubule alterations and muscle weakness in myotonic dystrophy. Nat. Med. *17*, 720–725.

Galili, T. (2015). dendextend: an R package for visualizing, adjusting and comparing trees of hierarchical clustering. Bioinformatics *31*, 3718–3720.

Goodman, V., and Azad, Bonni. (2019). Regulation of neuronal connectivity in the mammalian brain by chromatin remodeling. Current Opinion in Neurobiology *59*, 59–68.

Graber, T.E., Hébert-Seropian, S., Khoutorsky, A., David, A., Yewdell, J.W., Lacaille, J.C., and Sossin, W.S. (2013). Reactivation of stalled polyribosomes in synaptic plasticity. Proc. Natl. Acad. Sci. USA *110*, 16205–16210.

Greenblatt, E.J., and Spradling, A.C. (2018). Fragile X mental retardation 1 gene enhances the translation of large autism-related proteins. Science *361*, 709–712.

Groisman, I., Ivshina, M., Marin, V., Kennedy, N.J., Davis, R.J., and Richter, J.D. (2006). Control of cellular senescence by CPEB. Genes Dev. *20*, 2701–2712.

Guo, W., Molinaro, G., Collins, K.A., Hays, S.A., Paylor, R., Worley, P.F., Szumlinski, K.K., and Huber, K.M. (2016). Selective disruption of metabotropic glutamate receptor 5-homer interactions mimics phenotypes of fragile X syndrome in mice. J. Neurosci. *36*, 2131–2147.

Guo, W., Zhang, L., Christopher, D.M., Teng, Z.Q., Fausett, S.R., Liu, C., George, O.L., Klingensmith, J., Jin, P., and Zhao, X. (2011). RNA-binding protein FXR2 regulates adult hippocampal neurogenesis by reducing Noggin expression. Neuron *70*, 924–938.

Heise, C., Taha, E., Murru, L., Ponzoni, L., Cattaneo, A., Guarnieri, F.C., Montani, C., Mossa, A., Vezzoli, E., Ippolito, G., et al. (2017). eEF2K/eEF2 pathway controls the excitation/inhibition balance and susceptibility to epileptic seizures. Cereb. Cortex *27*, 2226–2248.

Heyer, E.E., Ozadam, H., Ricci, E.P., Cenik, C., and Moore, M.J. (2015). An optimized kit-free method for making strand-specific deep sequencing libraries from RNA fragments. Nucleic Acids Res. *43*, e2.

Houge, G., Rasmussen, I.H., and Hovland, R. (2012). Loss-of-function CNKSR2 mutation is a likely cause of non-syndromic X-linked intellectual disability. Mol. Syndromol. *2*, 60–63.

Huber, K.M., Gallagher, S.M., Warren, S.T., and Bear, M.F. (2002). Altered synaptic plasticity in a mouse model of fragile X mental retardation. Proc. Natl. Acad. Sci. U S A *99*, 7746–7750.

Huber, K.M., Kayser, M.S., and Bear, M.F. (2000). Role for rapid dendritic protein synthesis in hippocampal mGluR-dependent long-term depression. Science *288*, 1254–1257.

Huter, P., Arenz, S., Bock, L.V., Graf, M., Frister, J.O., Heuer, A., Peil, L., Starosta, A.L., Wohlgemuth, I., Peske, F., et al. (2017). Structural basis for polyproline-mediated ribosome stalling and rescue by the translation elongation factor EF-P. Mol. Cell *68*, 515–527.e6.

Ingolia, N.T. (2014). Ribosome profiling: new views of translation, from single codons to genome scale. Nat. Rev. Genet. *15*, 205–213.

Ingolia, N.T., Ghaemmaghami, S., Newman, J.R., and Weissman, J.S. (2009). Genome-wide analysis in vivo of translation with nucleotide resolution using ribosome profiling. Science *324*, 218–223.

Ingolia, N.T., Lareau, L.F., and Weissman, J.S. (2011). Ribosome profiling of mouse embryonic stem cells reveals the complexity and dynamics of mammalian proteomes. Cell *147*, 789–802.

Irimia, M., Weatheritt, R.J., Ellis, J.D., Parikshak, N.N., Gonatopoulos-Pournatzis, T., Babor, M., Quesnel-Vallières, M., Tapial, J., Raj, B., O'Hanlon, D., et al. (2014). A highly conserved program of neuronal microexons is misregulated in autistic brains. Cell *159*, 1511–1523.

Ishizuka, A., Siomi, M.C., and Siomi, H. (2002). A Drosophila fragile X protein interacts with components of RNAi and ribosomal proteins. Genes Dev. *16*, 2497–2508.

Kanai, Y., Dohmae, N., and Hirokawa, N. (2004). Kinesin transports RNA: isolation and characterization of an RNA-transporting granule. Neuron *43*, 513–525.

Khandjian, E.W., Corbin, F., Woerly, S., and Rousseau, F. (1996). The fragile X mental retardation protein is associated with ribosomes. Nat. Genet. *12*, 91–93.

Khandjian, E.W., Huot, M.E., Tremblay, S., Davidovic, L., Mazroui, R., and Bardoni, B. (2004). Biochemical evidence for the association of fragile X mental retardation protein with brain polyribosomal ribonucleoparticles. Proc. Natl. Acad. Sci. USA *101*, 13357–13362.

Kim, S., Kim, H., Fong, N., Erickson, B., and Bentley, D.L. (2011). Pre-mRNA splicing is a determinant of histone H3K36 methylation. Proc. Natl. Acad. Sci. USA *108*, 13564–13569.

Kolasinska-Zwierz, P., Down, T., Latorre, I., Liu, T., Liu, X.S., and Ahringer, J. (2009). Differential chromatin marking of introns and expressed exons by H3K36me3. Nat. Genet. *41*, 376–381.

Kolde, R. (2015). *Pheatmap: pretty heatmaps*. R Package Version 1.0.10. (CRAN), https://CRAN.R-project.org/package=pheatmap.

Korb, E., Herre, M., Zucker-Scharff, I., Gresack, J., Allis, C.D., and Darnell, R.B. (2017). Excess translation of epigenetic regulators contributes to fragile X syndrome and is alleviated by Brd4 inhibition. Cell *170*, 1209–1223.e20.

Krichevsky, A.M., and Kosik, K.S. (2001). Neuronal RNA granules: a link between RNA localization and stimulation-dependent translation. Neuron *32*, 683–696.

Krogan, N.J., Kim, M., Tong, A., Golshani, A., Cagney, G., Canadien, V., Richards, D.P., Beattie, B.K., Emili, A., Boone, C., et al. (2003). Methylation of histone H3 by Set2 in Saccharomyces cerevisiae is linked to transcriptional elongation by RNA polymerase II. Mol. Cell. Biol. *23*, 4207–4218.

Lai, M.C., Bechy, A.L., Denk, F., Collins, E., Gavriliouk, M., Zaugg, J.B., Ryan, B.J., Wade-Martins, R., and Caffrey, T.M. (2017). Haplotype-specific MAPT exon 3 expression regulated by common intronic polymorphisms associated with Parkinsonian disorders. Mol. Neurodegener. *12*, 79.

Lee, J.A., Damianov, A., Lin, C.H., Fontes, M., Parikshak, N.N., Anderson, E.S., Geschwind, D.H., Black, D.L., and Martin, K.C. (2016). Cytoplasmic Rbfox1 regulates the expression of synaptic and autism-related genes. Neuron *89*, 113–128.

Lee, S., Liu, B., Lee, S., Huang, S.X., Shen, B., and Qian, S.B. (2012). Global mapping of translation initiation sites in mammalian cells at single-nucleotide resolution. Proc. Natl. Acad. Sci. U S A *109*, E2424–E2432.

Liu, B., Li, Y., Stackpole, E.E., Novak, A., Gao, Y., Zhao, Y., Zhao, X., and Richter, J.D. (2018). Regulatory discrimination of mRNAs by FMRP controls mouse adult neural stem cell differentiation. Proc. Natl. Acad. Sci. USA *115*, E11397–E11405.

Liu, B., Molinaro, G., Shu, H., Stackpole, E.E., Huber, K.M., and Richter, J.D. (2019). Optimization of ribosome profiling using low-input brain tissue from fragile X syndrome model mice. Nucleic Acids Res. *47*, e25.

Lumish, H.S., Wynn, J., Devinsky, O., and Chung, W.K. (2015). Brief report: SETD2 mutation in a child with autism, intellectual disabilities and epilepsy. J. Autism Dev. Disord. *45*, 3764–3770.

Luo, Y., Shan, G., Guo, W., Smrt, R.D., Johnson, E.B., Li, X., Pfeiffer, R.L., Szulwach, K.E., Duan, R., Barkho, B.Z., et al. (2010). Fragile x mental retardation protein regulates proliferation and differentiation of adult neural stem/progenitor cells. PLoS Genet. *6*, e1000898.

Mallardo, M., Deitinghoff, A., Müller, J., Goetze, B., Macchi, P., Peters, C., and Kiebler, M.A. (2003). Isolation and characterization of Staufen-containing ribonucleoprotein particles from rat brain. Proc. Natl. Acad. Sci. USA *100*, 2100–2105.

Maurin, T., Lebrigand, K., Castagnola, S., Paquet, A., Jarjat, M., Popa, A., Grossi, M., Rage, F., and Bardoni, B. (2018). HITS-CLIP in various brain areas reveals new targets and new modalities of RNA binding by fragile X mental retardation protein. Nucleic Acids Res. *46*, 6344–6355.

McCamphill, P.K., Farah, C.A., Anadolu, M.N., Hoque, S., and Sossin, W.S. (2015). Bidirectional regulation of eEF2 phosphorylation controls synaptic plasticity by decoding neuronal activity patterns. J. Neurosci. *35*, 4403–4417.

Neri, F., Rapelli, S., Krepelova, A., Incarnato, D., Parlato, C., Basile, G., Maldotti, M., Anselmi, F., and Oliviero, S. (2017). Intragenic DNA methylation prevents spurious transcription initiation. Nature *543*, 72–77.

Nosyreva, E.D., and Huber, K.M. (2006). Metabotropic receptor-dependent long-term depression persists in the absence of protein synthesis in the mouse model of fragile X syndrome. J. Neurophysiol. *95*, 3291–3295.

Oertlin, C., Lorent, J., Murie, C., Furic, L., Topisirovic, I., and Larsson, O. (2019). Generally applicable transcriptome-wide analysis of translation using anota2se. Nucleic Acids Research *47*, e70.

Parikshak, N.N., Swarup, V., Belgard, T.G., Irimia, M., Ramaswami, G., Gandal, M.J., Hartl, C., Leppa, V., Ubieta, L.T., Huang, J., et al. (2016). Genome-wide changes in lncRNA, splicing, and regional gene expression patterns in autism. Nature *540*, 423–427.

Park, S., Park, J.M., Kim, S., Kim, J.A., Shepherd, J.D., Smith-Hicks, C.L., Chowdhury, S., Kaufmann, W., Kuhl, D., Ryazanov, A.G., Huganir, R.L., Linden, D.J., and Worley, P.F. (2008). Elongation factor 2 and fragile X mental retardation protein control the dynamic translation of Arc/Arg3.1 essential for mGluR-LTD. Neuron *59*, 70–83.

Parras, A., Anta, H., Santos-Galindo, M., Swarup, V., Elorza, A., Nieto-González, J.L., Picó, S., Hernández, I.H., Díaz-Hernández, J.I., Belloc, E., et al.

(2018). Autism-like phenotype and risk gene mRNA deadenylation by CPEB4 mis-splicing. Nature *560*, 441–446.

Quesnel-Vallières, M., Dargaei, Z., Irimia, M., Gonatopoulos-Pournatzis, T., Ip, J.Y., Wu, M., Sterne-Weiler, T., Nakagawa, S., Woodin, M.A., Blencowe, B.J., and Cordes, S.P. (2016). Misregulation of an activity-dependent splicing network as a common mechanism underlying autism spectrum disorders. Mol. Cell *64*, 1023–1034.

Quesnel-Vallières, M., Weatheritt, R.J., Cordes, S.P., and Blencowe, B.J. (2019). Autism spectrum disorder: insights into convergent mechanisms from transcriptomics. Nat. Rev. Genet. *20*, 51–63.

Raj, B., and Blencowe, B.J. (2015). Alternative splicing in the mammalian nervous system: recent insights into mechanisms and functional roles. Neuron *87*, 14–27.

Ramírez, F., Ryan, D.P., Grüning, B., Bhardwaj, V., Kilpert, F., Richter, A.S., Heyne, S., Dündar, F., and Manke, T. (2016). deepTools2: a next generation web server for deep-sequencing data analysis. Nucleic Acids Res. *44* (*W1*), W160–W165.

Richter, J.D., Bassell, G.J., and Klann, E. (2015). Dysregulation and restoration of translational homeostasis in fragile X syndrome. Nat. Rev. Neurosci. *16*, 595–605.

Robinson, M.D., McCarthy, D.J., and Smyth, G.K. (2010). edgeR: a Bioconductor package for differential expression analysis of digital gene expression data. Bioinformatics *26*, 139–140.

Rockenstein, E.M., McConlogue, L., Tan, H., Power, M., Masliah, E., and Mucke, L. (1995). Levels and alternative splicing of amyloid β protein precursor (APP) transcripts in brains of APP transgenic mice and humans with Alzheimer's disease. J. Biol. Chem. *270*, 28257–28267.

Santoro, M.R., Bray, S.M., and Warren, S.T. (2012). Molecular mechanisms of fragile X syndrome: a twenty-year perspective. Annu. Rev. Pathol. *7*, 219–245.

Scheetz, A.J., Nairn, A.C., and Constantine-Paton, M. (2000). NMDA receptor-mediated control of protein synthesis at developing synapses. Nat. Neurosci. *3*, 211–216.

Schuller, A.P., Wu, C.C., Dever, T.E., Buskirk, A.R., and Green, R. (2017). eIF5A functions globally in translation elongation and termination. Mol. Cell *66*, 194–205.e5.

Shen, S., Park, J.W., Lu, Z.X., Lin, L., Henry, M.D., Wu, Y.N., Zhou, Q., and Xing, Y. (2014). rMATS: robust and flexible detection of differential alternative splicing from replicate RNA-Seq data. Proc. Natl. Acad. Sci. USA *111*, E5593–E5601.

Smith, R.M., and Sadee, W. (2011). Synaptic signaling and aberrant RNA splicing in autism spectrum disorders. Front. Synaptic Neurosci. *3*, 1.

Stefani, G., Fraser, C.E., Darnell, J.C., and Darnell, R.B. (2004). Fragile X mental retardation protein is associated with translating polyribosomes in neuronal cells. J. Neurosci. *24*, 7272–7276.

Sutton, M.A., Taylor, A.M., Ito, H.T., Pham, A., and Schuman, E.M. (2007). Postsynaptic decoding of neural activity: eEF2 as a biochemical sensor coupling miniature synaptic transmission to local protein synthesis. Neuron *55*, 648–661.

Tabet, R., Moutin, E., Becker, J.A., Heintz, D., Fouillen, L., Flatter, E., Krężel, W., Alunni, V., Koebel, P., Dembélé, D., et al. (2016). Fragile X Mental Retardation Protein (FMRP) controls diacylglycerol kinase activity in neurons. Proc. Natl. Acad. Sci. USA *113*, E3619–E3628.

Thomson, S.R., Seo, S.S., Barnes, S.A., Louros, S.R., Muscas, M., Dando, O., Kirby, C., Wyllie, D.J.A., Hardingham, G.E., Kind, P.C., and Osterweil, E.K. (2017). Cell-type-specific translation profiling reveals a novel strategy for treating fragile X syndrome. Neuron *95*, 550–563.e5.

Tiedemann, R.L., Hlady, R.A., Hanavan, P.D., Lake, D.F., Tibes, R., Lee, J.H., Choi, J.H., Ho, T.H., and Robertson, K.D. (2016). Dynamic reprogramming of DNA methylation in SETD2-deregulated renal cell carcinoma. Oncotarget *7*, 1927–1946.

Udagawa, T., Farny, N.G., Jakovcevski, M., Kaphzan, H., Alarcon, J.M., Anilkumar, S., Ivshina, M., Hurt, J.A., Nagaoka, K., Nalavadi, V.C., et al. (2013). Genetic and acute CPEB1 depletion ameliorate fragile X pathophysiology. Nat. Med. *19*, 1473–1477.

van Bokhoven, H. (2011). Genetic and epigenetic networks in intellectual disabilities. Annu. Rev. Genet. *45*, 81–104.

Van Driesche, S.J., Sawicka, K., Zhang, C., Hung, S.K.Y., Park, C.Y., Fak, J.J., Yang, C., Darnell, R.B., and Darnell, J.C. (2019). FMRP binding to a ranked subset of long genes is revealed by coupled CLIP and TRAP in specific neuronal cell types. bioRxiv. https://doi.org/10.1101/762500.

Wang, C.X., Cui, G.S., Liu, X., Xu, K., Wang, M., Zhang, X.X., Jiang, L.Y., Li, A., Yang, Y., Lai, W.Y., et al. (2018). METTL3-mediated m 6 A modification is required for cerebellar development. PLoS Biol. *16*, e2004880.

Ward, J.H., Jr. (1963). Hierarchical grouping to optimize an objective function. J. Am. Stat. Assoc. *58*, 236–244.

Waung, M.W., and Huber, K.M. (2009). Protein translation in synaptic plasticity: mGluR-LTD, Fragile X. Curr. Opin. Neurobiol. *19*, 319–326.

Wobst, H.J., Denk, F., Oliver, P.L., Livieratos, A., Taylor, T.N., Knudsen, M.H., Bengoa-Vergniory, N., Bannerman, D., and Wade-Martins, R. (2017). Increased 4R tau expression and behavioural changes in a novel MAPT-N296H genomic mouse model of tauopathy. Sci. Rep. *7*, 43198.

Xu, S., Grullon, S., Ge, K., and Peng, W. (2014). Spatial clustering for identification of ChIP-enriched regions (SICER) to map regions of histone methylation patterns in embryonic stem cells. Methods Mol. Biol. *1150*, 97–111.

Yu, G., Wang, L.-G., Han, Y., and He, Q.-Y. (2012). clusterProfiler: an R package for comparing biological themes among gene clusters. OMICS *16*, 284–287.

Yukselen, O., Turkyilmaz, O., Ozturk, A., Garber, M., and Kucukural, A. (2019). DolphinNext: a distributed data processing platform for high throughput genomics. bioRxiv. https://doi.org/10.1101/689539.

STAR★METHODS

KEY RESOURCES TABLE

REAGENT or RESOURCE	SOURCE	IDENTIFIER
Antibodies		
SETD2 Rabbit pAb-Polyclonal Antibodies	ABclonal	Cat# A11271; RRID: AB_2758486
Lamin A/C Mouse Monoclonal Antibody (4A7)	Thermo Fisher	Cat# 14-9688-80; RRID: AB_2572956
HRP conjugated antimouse secondary antibody	Jackson Immunoresearch	Cat# 115-035-174; RRID: AB_2338512
Rabbit polyclonal to Lamin B1	Abcam	Cat# ab16048; RRID: AB_443298
Anti-FMRP Rabbit polyclonal antibody	Abcam	Cat# ab17722; RRID: AB_2278530
HRP conjugated mouse anti-rabbit secondary antibody	Jackson Immunoresearch	Cat# 211-032-171; RRID: AB_2339149
Anti-α-Tubulin mouse Monoclonal antibody	Sigma	Cat# T5168; RRID: AB_477579
Anti-Rpl4 mouse monoclonal antibody	Proteintech	Cat# 67028-1-Ig
Recombinant Anti-RENT1/hUPF1 antibody [EP4682]	Abcam	Cat# 133564
Anti-MAP2 mouse monoclonal Antibody, clone AP20	Millipore	Cat# AB5543; RRID: AB_571049
Anti-eEF2 polyclonal rabbit Antibody	Cell Signaling Technology	Cat# 2332; RRID: AB_10693546
Anti- GAPDH (14C10) Rabbit monocloanal Antibody	Cell Signaling Technology	Cat# 2118; RRID: AB_561053
Anti-MRPS18B Rabbit Polyclonal Antibody	Proteintech	Cat# 16139-1-AP; RRID: AB_2146368
Anti-S6 Ribosomal Protein (5G10) Rabbit monoclonal antibody	Cell Signaling Technology	Cat# 2217; RRID: AB_331355
Anti-IgG mouse polyclonal antibody	Sigma	Cat# 12-371; RRID: AB_145840
Anti-Histone H3 (tri methyl K36) Rabbit polyclonal antibody	Abcam	Cat# ab9050; RRID: AB_306966
Chemicals, Peptides, and Recombinant Proteins		
Cycloheximide solution	Sigma	Cat#C4859
homoHarringtonine	LKT laboratories	Cat#H0169-5
Turbo DNaseI	Ambion	Cat#AM2238
RNase A	Sigma	Cat#R4875
RNase T1	Thermo Fisher Scientific	Cat#EN0542
SUPERase In RNase inhibitor	Ambion	Cat#AM2694
RiboZero	Illumina	Cat#MRZG12324
5 nm miRCat®-33 Conversion Oligos Pack15nm	IDT	Cat#51-01-13-10
SuperScript III	Invitrogen	Cat#18080-044
CircLigase	Epicenter	Cat#CL4115K
Dynabeads MyOne Streptavidin C1	Invitrogen	Cat#65001
KAPA Library Amplification Kit	Kapa Biosystems	Cat#KK2611
AMPure XP beads	Beckman Coulter	Cat#A63880
NextSeq 500/550 High Output Kit v2 (75bp single-end runs)	Illumina	Cat#FC-404-2005
NextSeq 500/550 High Output Kit v2 (80bp pair-end runs)	Illumina	Cat#FC-404-2002
NEXTflex® Rapid Directional qRNA-Seq Kit (24 barcodes) - Set A/B	biooscientific	Cat#NOVA-5130-03D
Critical Commercial Assays		
Qubit RNA HS Assay Kit	Fisher scientific	Cat#Q32852
Deposited Data		
Raw and analyzed data	This paper	GEO: GSE143333
Mouse reference genome NCBI build 38,mm10	Genome Reference Consortium	https://www.ncbi.nlm.nih.gov/projects/genome/assembly/grc/mouse/

(*Continued on next page*)

Continued		
REAGENT or RESOURCE	SOURCE	IDENTIFIER
Experimental Models: Cell Lines		
Immortalized Mouse Embryonic Fibroblasts (MEFs)	C57BL/6N wild-type or *Fmr1* KO mice	NA
Experimental Models: Organisms/Strains		
Mouse C57BL/6 wild-type	Jackson lab	Cat# JAX:000664; RRID: IMSR_JAX:000664
$Fmr1^{tm1Cgr}/Fmr1^{tm1Cgr}$ Mus musculus, backcrossed for more than 10 generations on a C57BL/6 background	Dr. Stephen T. Warren	Cat# 2665400; RRID: MGI:2665400
Oligonucleotides		
See Table S1, sheet 5	NA	NA
Software and Algorithms		
DolphinNext	Yukselen et al., 2019	NA
clusterProfiler (3.10.1)	Yu et al., 2012	NA
hclust	Galili, 2015	NA
pheatmap	Kolde, 2015	NA
anota2seq (1.0.0)	Oertlin et al., 2019	NA
SICER v1.1	Xu et al., 2014	NA
rMATS package v3.2.5	Shen et al., 2014	NA
deepTools	Ramírez et al., 2016	NA

LEAD CONTACT AND MATERIALS AVAILABILITY

Further information and requests for resources and reagents should be directed to and will be fulfilled by the Lead Contact, Joel Richter (joel.richter@umassmed.edu). This study did not generate new unique reagents.

EXPERIMENTAL MODEL AND SUBJECT DETAILS

All experiments were approved by the Institutional Animal Care and Use Committee at University of Texas Southwestern and University of Massachusetts Medical School and conducted in accordance with the National Institutes of Health Principles of Laboratory Animal Care. *Fmr1* KO mice were obtained from Dr. Stephen T. Warren and backcrossed for more than 10 generations on a C57BL/6 background. Food and water were provided *ad libitum*, and mice were kept on a 12 h light/dark cycle (7am-7pm light period). Pups were kept with their dams until weaning at postnatal day 21. After weaning, mice were group housed (maximum of 5 per cage) by sex. Cages were maintained in ventilated racks in temperature (20-21°C) controlled rooms. P28-35 wild-type or *Fmr1* KO male mice littermates were used in this study.

Cell culture

Immortalized Mouse Embryonic Fibroblasts (MEFs) were derived from C57BL/6N wild-type or *Fmr1* KO mice as described earlier (Groisman et al., 2006. Immortalized MEF cells were cultured in DMEM (Dulbecco's Modified Eagle's Medium, GIBCO) with 10% fetal bovine serum using the 3T3 culture protocol and cells derived from Passage number 31 onward were used for western blot analysis.

METHOD DETAILS

Mouse acute brain slice preparation

Transverse hippocampal or hippocampal-cortical brain slices were acutely prepared from P28-35 C57BL/6N wild-type or *Fmr1* KO male mice littermates as previously described (Guo et al., 2016). Briefly, mice were anesthetized with ketamine (125 mg/kg)/xylazine (25 mg/kg) and transcardially perfused with chilled (4°C) sucrose dissection buffer containing the following (in mM): 2.6 KCl, 1.25 NaH_2PO_4, 26 $NaHCO_3$, 0.5 $CaCl_2$, 5 $MgCl_2$, 212 mM sucrose, and 10 dextrose aerated with 95% O_2/5% CO_2. Transverse hippocampal slices (400μm) were obtained on a Leica VT1200S slicer. For ribosomal profiling experiments (Figure 1), CA3 was cut off to enrich for CA1 and for each biological replicate (n), 8-10 slices from 6-8 mice/genotype were pooled. Slices were recovered and maintained at 30°C for 3–4 h in artificial cerebrospinal fluid (ACSF) which contained the following (in mM): 119 NaCl, 2.5 KCl, 2 $CaCl_2$, 1 $MgCl_2$, 26 $NaHCO_3$, 1 NaH_2PO_4 and 11 D-glucose aerated with 95%/O_2/5% CO_2 to pH 7.4. Slices were then treated with cycloheximide (100 μg/ml) in ACSF, 4°C, snap-frozen on dry ice/EtOH bath, and stored at −80°C. For homoharringtonine (HHT) experiments (Figures 3, 4, and 5), cortical-hippocampal slices were recovered 3-4 hours in ACSF and then treated with HHT (20 μM) (Tocris) or 0.05%

DMSO (vehicle) for different times (0, 5, 10, 30, 60 min). At the end of the incubation time, slices were snap/frozen on dry ice/EtOH bath and stored at −80 C. Ten slices from 2-3 mice/genotype were pooled for each biological replicate.

Sucrose gradients of hippocampal slices for steady-state ribosome profiling

Frozen, isolated CA1 hippocampal slices were thawed in ice-cold homogenization buffer (20mM Tris-HCl pH7.4, 5mM $MgCl_2$, 100mM KCl, 1mM DTT, 100 μg/ml CHX (cycloheximide), 25U/ml Turbo DNaseI (Ambion, #AM2238), 1X EDTA-free protease inhibitor (Roche), avoiding detergent in nuclease-free water) on ice for 5min. Wide orifice tips were used to transfer slices to a pre-chilled detergent-free Dounce homogenizer. Tissues were slowly homogenized by hand (20 strokes of loose pestle A, and 20 strokes of tight pestle B). Homogenates were carefully transferred to clean 1.5ml tubes with clean glass Pasteur pipets and bulbs. 1% NP-40 was added to the homogenates and incubated on ice for 10min. Homogenates were clarified by centrifugation at 2,000 g 4°C for 10min. The supernatants were collected and clarified again by centrifugation at 20,000 g 4°C for 10min. The supernatants were collected, and the amounts of nucleic acid were measured by Nanodrop (A_{260} units). For each sample, cytoplasmic RNA for RNA-seq was purified from one-fourth of the lysate with TRIzol LS reagent (Invitrogen, #10296028). The other three-fourths of the lysate was digested with 100ng RNase A (Sigma, # R4875) and 60U RNase T1 (Thermo Fisher Scientific, #EN0542) per A_{260} at 25°C for 30 min and stopped by chilling on ice and adding 50U SUPERase In RNase inhibitor (Ambion, #AM2694). Digested lysates were applied to 10%–50% (w/v) sucrose gradients prepared in 1X polysome buffer (20mM Tris-HCl pH7.4, 5mM $MgCl_2$, 100mM KCl, 1mM DTT, 100 μg/ml CHX in nuclease-free water). After the ultracentrifugation in a SW41Ti rotor (Beckman Coulter) at 35,000 rpm (avg 151,263 g) 4°C for 2.5 h, gradients were fractionated at 1.5 ml/min and 12 s collection intervals through a fractionation system (Brandel) that continually monitored A_{260} values. Monosome fractions were identified, pooled, and extracted with TRIzol LS.

Sucrose gradients of cortical-hippocampal slices for run-off ribosome profiling

Frozen cortical-hippocampal slices were thawed in ice-cold lysis buffer (20mM Tris-HCl pH7.4, 5mM $MgCl_2$, 100mM KCl, 1mM DTT, 100 μg/ml CHX, 25U/ml Turbo DNaseI, 1X EDTA-free protease inhibitor, 1% NP-40, in nuclease-free water) on ice for 5min. Tissues were dissociated by pipetting and further trituration through 25G needle for 10 times. Lysates were incubated on ice for 10min and then clarified by centrifugation at 2,000 g 4°C for 10min. The supernatants were collected and clarified again by centrifugation at 20,000 g 4°C for 10min. The supernatants were collected, and the amounts of nucleic acid were measured with Qubit HS RNA assays. Lysates containing ~40μg RNA were digested with 600ng RNase A (Ambion, #AM2270) + 75U RNase T1 (Thermo Fisher Scientific, #EN0542) /μg RNA in 0.3ml at 25°C for 30min and stopped by chilling on ice and adding 50U SUPERase In RNase inhibitor. Digested lysates were applied to 10%–50% (w/v) sucrose gradients similarly as above.

Sucrose gradients of cortical-hippocampal slices for polysome profiling

Frozen cortical-hippocampal slices were thawed in ice-cold homogenization buffer on ice for 5min. Wide orifice tips were used to transfer slices to a pre-chilled detergent-free Dounce homogenizer. Tissues were gently homogenized by hand (3 strokes of loose pestle A, and 7 strokes of tight pestle B). Homogenates were carefully transferred to clean 1.5ml tubes with clean glass Pasteur pipets and bulbs. Homogenates were clarified by centrifugation at 2,000 g 4°C for 10min. The supernatants were collected and clarified again by centrifugation at 10,000 g 4°C for 10min. The supernatants were collected, and the amounts of nucleic acid were measured with Nanodrop (A_{260} units). 1% NP-40 was added to the homogenates and incubated on ice for 10min. ~$1A_{260}$ unit of lysate was saved for the input RNA. ~5 A_{260} units of lysate were applied to 15%–45% (w/w) sucrose gradients prepared in 1X polysome buffer and with the lower block mark and long cap. After the ultracentrifugation in a SW41Ti rotor (Beckman Coulter) at 35,000 rpm (avg 151,263 g) 4°C for 2 h, gradients were fractionated at 1.5 ml/min and 20 s collection intervals through a fractionation system (Brandel) that continually monitored A_{260} values. Some gradients were treated with RNase A prior to centrifugation.

Ribosome profiling

Ribosome profiling libraries were prepared following the published protocols (Heyer et al., 2015). Briefly, rRNA was depleted from the purified monosomal RNA with RiboZero (Illumina, #MRZG12324). Remaining RNA samples were separated on a 15% TBU gel (National Diagnostics, #EC-833) and the ribosome footprints were size-selected between the 26 and 34nt markers. RNA was eluted from the crushed gel pieces in RNA elution buffer (300mM NaOAc pH5.5, 1mM EDTA, 0.25% SDS) at room temperature overnight, filtered with Spin-X Centrifuge Tube Filters (Corning, #8162) and precipitated with equal volume of isopropanol. Recovered RNA was dephosphorylated with T4 Polynucleotide Kinase (NEB, #M0201S) and ligated with preadenylated adaptor in miRCat®-33 Conversion Oligos Pack (IDT) using T4RNL2Tr.K227Q ligase (NEB, #M0351L). Reverse transcription (RT) was performed with primers containing 5nt-barcodes and 8nt-unique molecular identifiers (UMIs) and SuperScript III (Invitrogen, #18080-044) in 1X first-strand buffer without $MgCl_2$ (50 mM Tris-HCl, pH 8.3, 75 mM KCl). RT products were separated on a 10% TBU gel and the 130-140nt region was selected. cDNA was eluted in DNA elution buffer (10mM Tris pH 8.0, 300mM NaCl, 1mM EDTA) at room temperature overnight, filtered, and precipitated with isopropanol. Purified cDNA was circularized with CircLigase (Epicenter, #CL4115K). Except for the RNase titration samples, cDNA derived from remaining rRNA was hybridized to biotin-labeled antisense probes (IDT) and further depleted with Dynabeads MyOne Streptavidin C1 (Invitrogen, #65001). Optimal PCR cycle number was determined empirically by test PCR reactions with titrated cycle numbers. Final PCR amplification was performed with KAPA Library Amplification Kit (Kapa Biosystems, #KK2611) and 180-190bp products were size-selected on an 8% TBE gel. DNA was eluted in DNA elution buffer, filtered, and precipitated with

isopropanol. The final library DNA was purified with AMPure XP beads (Beckman Coulter, #A63880). Oligos used for the library preparation are listed in Table S2.

In parallel, input RNA samples were processed similarly as the ribosome footprints except the following steps. After rRNA depletion, input RNA mixed with an equal volume of 2x alkaline fragmentation solution (2 mM EDTA, 10 mM Na_2CO_3, 90 mM NaHCO3, pH ~9.3) and heated at 95°C for 15min to achieve an average fragment length of ~140nt. Fragmented RNA samples were separated on a 10% TBU gel and size-selected between the 100 and 150nt markers. RT products were separated on a 10% TBU gel and the 200-250nt region was selected. Antisense probe depletion was omitted for input RNA samples. 260-300bp final PCR products were size-selected on an 8% TBE gel.

The size distributions of final libraries were measured by Fragment Analyzer (Advanced Analytical, performed by Molecular Biology Core Labs at UMMS). The concentrations were quantified with KAPA Library Quantification Kit (Kapa Biosystems, #KK4835). Libraries were pooled with equal molar ratios, denatured, diluted, and sequenced with NextSeq 500/550 High Output Kit v2 (Illumina, 75bp single-end runs, #FC-404-2005) on a Nextseq500 sequencer (Illumina).

RNA-seq for polysome fractions

Based on the FMRP signals in the immunoblotting of gradient fractions, medium and heavy fractions were identified, pooled, and extracted with TRIzol LS together with saved input lysates. RNA samples were quantified with Qubit HS RNA assay kit and the integrity was examined with Fragment Analyzer. 200ng RNA was used for BIOO Rapid directional qRNA-seq library preparation following the manufacturer's instructions. 12 cycles were used for the final PCR amplification. The libraries were quantified with KAPA Library Quantification Kit and the quality was examined with Fragment Analyzer. Libraries were pooled with equal molar ratios, denatured, diluted, and sequenced with NextSeq 500/550 High Output Kit v2 (Illumina, 80bp pair-end runs for RNA-seq, #FC-404-2002) on a Nextseq500 sequencer (Illumina).

Western blotting

Hippocampi were homogenized at 4°C in RIPA buffer. Protein complexes were released by sonication at 4°C and the extract was centrifuged at 13,200 rpm for 10 min at 4°C and the supernatant collected. Protein concentration was determined by BCA reagent. Proteins (10 μg) were diluted in SDS-bromophenol blue reducing buffer with 40 mM DTT and analyzed using western blotting with the following antibodies: SETD2 (ABclonal, A11271) and Lamin AC (Thermo Fisher, 14-9688-80). After incubation in primary antibody, immunoblots were incubated with HRP-conjugated secondary antibodies (Jackson Immunoresearch) and developed by Clarity ECL substrate (Biorad). For western blots for SETD2 detection, Hippocampi or MEF cells were homogenized in Triton Extraction Buffer (TEB: PBS containing 0.5% Triton X 100 (v/v), 2 mM phenylmethylsulfonyl fluoride (PMSF), 0.02% (w/v) NaN_3), centrifuged at 2000 rpm. The pellet containing the nuclei was resuspended in RIPA Buffer and Protein complexes were released by sonication at 4°C. Protein concentration was determined by BCA reagent. Proteins (30 μg) were diluted in SDS-bromophenol blue reducing buffer with 40 mM DTT and analyzed using western blotting with the following antibodies: SETD2 (ABclonal, A11271) and Lamin AC (Thermo Fisher, 14-9688-80) or Lamin B1 (Abcam, ab16048). After incubation in primary antibody, immunoblots were incubated with HRP-25 conjugated secondary antibodies (Jackson Immunoresearch) and developed by Clarity ECL. For sucrose gradient fractions, 60μl samples were mixed with 20μl 4X SDS loading dye (240mM Tris-HCl pH 6.8, 5% beta-mercaptoethanol, 8% SDS, 40% glycerol, 0.04% bromophenol blue) and boiled at 95°C for 10min. Samples were briefly heated at 95°C again for 30sec immediately before loading on 10% SDS-PAGE gel (35 μl/sample). Separated proteins were transferred to PVDF membranes at constant 90 mA 4°C for 16 h. Membranes were blocked with 5% non-fat milk in 1X TBST at room temperature for 1hour and incubated with primary antibody at 4°C overnight. FMRP (Abcam, 1: 2000), Tubulin (Sigma, 1:5000), Rpl4 (Proteintech, 1:5000), UPF1 (Abcam, 1: 5000), MAP2 (Millipore, 1:2000), eEF2 (Cell signaling, 1:2000), GAPDH (Cell signaling, 1:2000), MRPS18B (Proteintech, 1:2000) and Rps6 (Cell signaling, 1:4000) were diluted in 1X TBST with 5% non-fat milk. Membranes were washed three times for 10min with 1XTBST and incubated with anti-rabbit or anti-mouse secondary antibodies (Jackson, 1:10000) at room temperature for 1hour. Membranes were washed three times for 10min with 1XTBST, developed with ECL-Plus (Piece), and scanned with GE Amersham Imager

Chromatin immunoprecipitation Sequencing (ChIP-Seq)

ChIP was performed as previously described (Cotney and Noonan, 2015). Briefly, hippocampal tissue was isolated from 4 adult mice (P35) per genotype and minced into tissue < $0.5mm^3$ in 250ul of ice-cold PBS with protease inhibitors. Tissue was cross-linked with 1% formaldehyde and rotated at room temperature for 15 min at 50 rpm and quenched with 150mm glycine for 10 min in a total volume of 1ml PBS. The supernatant was discarded after centrifugation at 2000 g for 10 min at 4°C and the pellet was resuspended in 300ul of chilled cell lysis buffer for 20 min on ice. Swollen pellets were homogenized using a glass Dounce homogenizer (2ml) with 40 strokes of a tight pestle on ice. Nuclei were harvested after centrifugation at 2000 g for 5min at 4°C and resuspended in 300ul ice-cold nuclear lysis buffer for 20min on ice. SDS was added to make a final concentration of 0.5%. Samples were sonicated on a Bioruptor® sonicator at high power settings for 9 cycles (sonication: 30 s on, 90 s off) of 15min each at 4°C at high power. Supernatants were collected after centrifugation at 16,000 g for 10 min at 4°C. The samples were diluted to bring the SDS concentration < 0.1%; 10% of each sample was reserved as input. The rest of the samples were divided into two and incubated with Protein G dynabeads coupled overnight at 4°C with either H3K36me3 (Abcam ab9050, 5 μg per ChIP) or IgG (Sigma 12-371, 5 μg per ChIP). After IP, beads were washed, and chromatin eluted in elution buffer for 20 min shaking at 65°C. IP and Input samples were de-crosslinked overnight at

65°C. RNase digestion for 1 hr. at 37°C and proteinase K treatment for 30 min at 55°C was performed. DNA was then purified with the QIAGEN PCR purification kit in 50ul elution buffer. For library preparation, purified input and IP DNA was end repaired using T4 DNA polymerase, Klenow polymerase and T4 Polynucleotide kinase from NEB at 20°C for 30 min. DNA was extracted using 35ul of the Agencourt Ampure XP beads and 'A' bases were added to the 3′ end using Klenow exonuclease (3′ to 5′ exo minus) from NEB for 30min at 37°C. DNA was purified using 60ul of the Agencourt Ampure XP beads and Illumina adaptor sequences were ligated to the DNA fragments using the Quick Ligase (NEB) for 15min at 20°C. The library was size-selected using 50ul of Agencourt Ampure XP beads. Using the multiplexing barcoded primers, the library was PCR amplified and purified using 50ul of the Agencourt Ampure XP beads and analyzed using a Fragment Analyzer (Advanced Analytical, performed by Molecular Biology Core Labs at UMMS). Libraries were pooled with equal molar ratios, denatured, diluted, and sequenced with NextSeq 500/550 High Output Kit v2.5 (Illumina, 75bp paired-end runs,) on a Nextseq500 sequencer (Illumina).

QUANTIFICATION AND STATISTICAL ANALYSIS

All grouped data are presented as mean ± s.e.m. All tests used to compare the samples are mentioned in the respective figure legends and corresponding text. When exact p values are not indicated, they are represented as follows: *, $p < 0.05$; **, $p < 0.01$; ***, $p < 0.001$; ****, p value < 0.0001; n.s., $p > 0.05$.

Ribosome profiling analysis

Individual samples were separated from the raw fastq files based on the barcode sequences. Adaptor sequences (TGGAATTCTCGGGTGCCAAGGAGATCGGAAGAGCGGTTCAGCAGGAATGCCGAGACCG) were removed with cutadapt (1.7.1). Trimmed fastq files were uploaded to the Dolphin platform (https://www.umassmed.edu/biocore/introducing-dolphin/) at the UMMS Bioinformatics Core for the mapping steps. Trimmed reads were quality filtered with Trimmomatic (0.32) and mapped to the mouse rRNA and then tRNA references with Bowtie2 (2.1.0). Unmapped reads were next mapped to the mm10 mouse genome with Tophat2 (2.0.9). Reads mapped to > 1 loci of the genome were classified as "multimapped" reads and discarded. PCR duplicates were marked based on the UMI sequences with custom scripts and only uniquely mapped reads without duplicates were retained with Samtools (0.0.19) for the downstream analyses. RPF length distribution, P-site offsets, and frame preference were calculated with plastid (0.4.8). Counts at each nucleotide position were extracted using P-sites of RPFs and 5′end of mRNA reads with +11 offset, normalized to the library size, averaged across replicates, and plotted along mRNA positions with custom scripts.

Steady-state differential translation analysis

Cleaned bam files were converted to fastq files with bedtools. For both ribosome profiling and RNA-seq, gene expression was quantified with RSEM (1.2.11) using the cleaned fastq files and Refseq (V69) mouse CDS without the first and last 30nt to avoid the translation initiation and termination peaks. Genes were filtered with minimum 10 reads across all replicates and then the read counts were batch-corrected with the Combat function in sva (3.24.4) using a full model matrix. Batch-corrected counts were normalized with trimmed mean of M values (TMM) method and used to identify differential expressed genes (DEGs) with anota2seq (1.0.0). Instead of the default setting, the priority of TE groups were set to be higher than that of mRNA only groups. A permutation test was performed to estimate the false discovery rate (FDR) with nominal p value < 0.01, which was 0.097. GO analysis was performed and plotted with clusterProfiler (3.10.1; Yu et al., 2012) using all genes past filtering in the dataset as the background.

Hierarchical clustering of ribosome run-off and gene ontology (GO) enrichment of each cluster

RPFs were mapped as described above and the most abundant isoform estimated by RSEM for each gene was selected as the representative transcript. For the metagene analysis, transcripts with CDS longer than 3000nt (n = 1401) were selected to ensure incomplete ribosome run-off after 10min HTT treatment. The read densities at each nucleotide position were normalized to the average density of the last 500nt of CDS and averaged using the P sites of RPFs. For visualization purposes, the curves were smoothed within a 90nt window. An arbitrary 0.8 threshold was used to estimate the relative run-off distances at 5 and 10min. A linear regression analysis between the HHT treatment time and ribosome run-off distances was performed to estimate the global elongation rate. To visualize the run-off patterns for individual transcripts, RPFs were normalized to the abundance of mitochondrial RPFs and plotted along the mRNA nucleotide positions. The same y-scale was used across the time-course, so the initiation peaks were truncated to reveal the patterns over CDS. Stalled ribosomes were quantified by RSEM by mapping RPFs to Refseq (V69) mouse CDS without the first and last 300nt to avoid the translation initiation and termination peaks after prolonged HTT treatment. Counts of RPFs were normalized to the length of CDS minus 600nt and the abundance of mitochondrial RPFs in that sample to calculate the RPK (Reads Per Kilobase of transcript) value for each transcript.

To categorize and group genes with distinct ribosome run-off patterns, the RPF of each gene at each time point was first normalized to time point 0. The Euclidean distance matrix was then calculated, followed by hierarchical clustering using Ward's agglomeration method (Ward, 1963). The clustering process was performed using the hclust (Galili, 2015), and the clustering heatmap was displayed using pheatmap (Kolde, 2015) in R. To test the reliability of clustering, analysis of group similarities (ANOSIM) test (Clarke, 1993) was performed using vegan (Dixon, 2003) in R with 1000 permutation times on both overall clusters and sub-clusters. The global pattern of each cluster was summarized using the corresponding median and standard deviation in each time point.

GO enrichment analysis for each sub-cluster were performed through clusterProfiler (Yu et al., 2012) using genes covered by run-off ribosome profiling as background. The statistical significance was adjusted using FDR. To remove redundancy in reporting, each reported GO term was required to have at least 25% of genes that were not associated to another term with a more significant p value.

Polysome fraction RNA-seq data analysis

Fastq files were uploaded to the Dolphin platform at the UMMS Bioinformatics Core for mapping and quantification. 9nt molecular labels were trimmed from both 5′ends of the pair-end reads and quality-filtered with Trimmomatic (0.32). Reads mapped to mouse rRNA by Bowtie2 (2.1.0) were filtered out. Cleaned reads were next mapped to the Refseq (V69) mouse transcriptome and quantified by RSEM (1.2.11).

Estimated counts on each gene were used for the differential gene expression analysis by DESeq2 (1.16.1). After the normalization by median of ratios method, only the genes with minimal 5 counts average across all samples were kept for the DEG analysis. Data were fit to a model of treatment+fraction+treatment:fraction+treatment:genotype:fraction and the treatmenthht.fractionheavy result was used to identify mRNA enriched or depleted in the heavy fractions after HTT treatment. $p < 0.05$ and 2-fold change were used as the cut-offs.

For the medium fractions after HHT treatment, *Fmr1* KO samples was directly compared to the WT samples and $p < 0.05$ was used as the cut-off for identifying DEGs. Steady-state ribosome profiling data of the decreased DEGs were compared to all the other genes to independently confirm whether these mRNAs indeed had fewer stalled ribosomes in *Fmr1* KO.

ChIP-Seq analysis

For ChIP-sequencing analysis, alignments were performed with Bowtie2 (2.1.0) using the mm10 genome, duplicates were removed with Picard and TDF files for IGV viewing were generated using a ChIP-seq pipeline from DolphinNext (Yukselen et al., 2019). The broad peaks for H3K36me3 ChIP-Seq were called using the SICER v1.1 package (Xu et al., 2014). H3K36me3 enriched islands were identified using the parameters set to a window size of 200bp, gap size 600bp and FDR cutoff of 1×10^{-3}, and the default value for the redundant rate cutoff. To analyze the H3K36me3 difference level between WT and FMRP KO, the reads count on each island of each replicate was first normalized to total mapped reads and then normalized to its corresponding input sample. The H3K36me3 difference level of each island is then calculated using both replicates in FMRP KO and WT groups; a negative binomial test is performed using edgeR (Robinson et al., 2010) to consider variability between replicates and differences between FMRP KO and WT groups. The islands with significantly different H3K36me3 levels are defined using a cut-off for fold change >2 and p value <0.05. Gene Ontology (GO) enrichment analysis was performed using the clusterProfiler package (Yu et al., 2012) to obtain GO terms related to Biological processes in the genes with differentially enriched islands in the *Fmr1* KO versus Wild-type. deepTools (Ramírez et al., 2016) was used to plot heatmaps and profiles for genic distribution of H3K36me3 ChIP signal. Samtools (0.1.19) was used for sorting and converting Bam files. RPGC (per bin) = number of reads per bin / scaling factor for 1x average coverage was used for normalization where the scaling factor was determined using sequencing depth: (total number of mapped reads x fragment length) / effective genome size. IGV tools (2.3.67) was used for visualizing TDF files and all tracks shown are normalized for total read coverage.

To quantify the H3K36me3 level at the 5′ and 3′ splicing sites of the SE, the read density at a region of ± 50nt at each splice site (total 100nt) and ± 150nt at each splice site (total 300nt) was normalized to the read density in the entire gene body, which controls for any fluctuations in total H3K36me3 at the respective genes between both genotypes (p value calculated using the Wilcox test for significance

Alternative splicing analysis

RNA-seq from hippocampal slices was used to analyze alternative splicing (AS) using the rMATS package v3.2.5 (Shen et al., 2014) with default parameters and reads were trimmed to 50bp. The Percent Spliced In (PSI) levels or the exon inclusion levels calculated by rMATS using a hierarchical framework. To calculate the difference in PSI between genotypes a likelihood-ratio test was used. AS events with an FDR < 5% and $|\text{deltaPSI}| \geq 5\%$ as identified using rMATS were used for further analysis. We included genes that had at least one read at the differential splice junction for both genotypes. GO enrichment analysis was done by the clusterProfiler package (Yu et al., 2012) to obtain GO term enrichment for the AS events. The genes with significant skipped exons were used for validation using RT-qPCR analysis. One ug of RNA from hippocampal tissue was used to generate cDNA using the Quantitech two-step cDNA synthesis kit. Primers were designed to overlap skipped/inclusion exon junctions and qPCR was performed using the Bio-Rad SYBR reagent on a Quantstudio3 instrument.

DATA AND CODE AVAILABILITY

Codes and scripts used for quantification analysis were written in Python or R and will be provided upon request to the Lead Contact.. The Gene Expression Omnibus (GEO) accession number for the data reported in this paper is GSE143333.

Cell Reports, Volume *30*

Supplemental Information

FMRP Control of Ribosome Translocation Promotes Chromatin Modifications and Alternative Splicing of Neuronal Genes Linked to Autism

Sneha Shah, Gemma Molinaro, Botao Liu, Ruijia Wang, Kimberly M. Huber, and Joel D. Richter

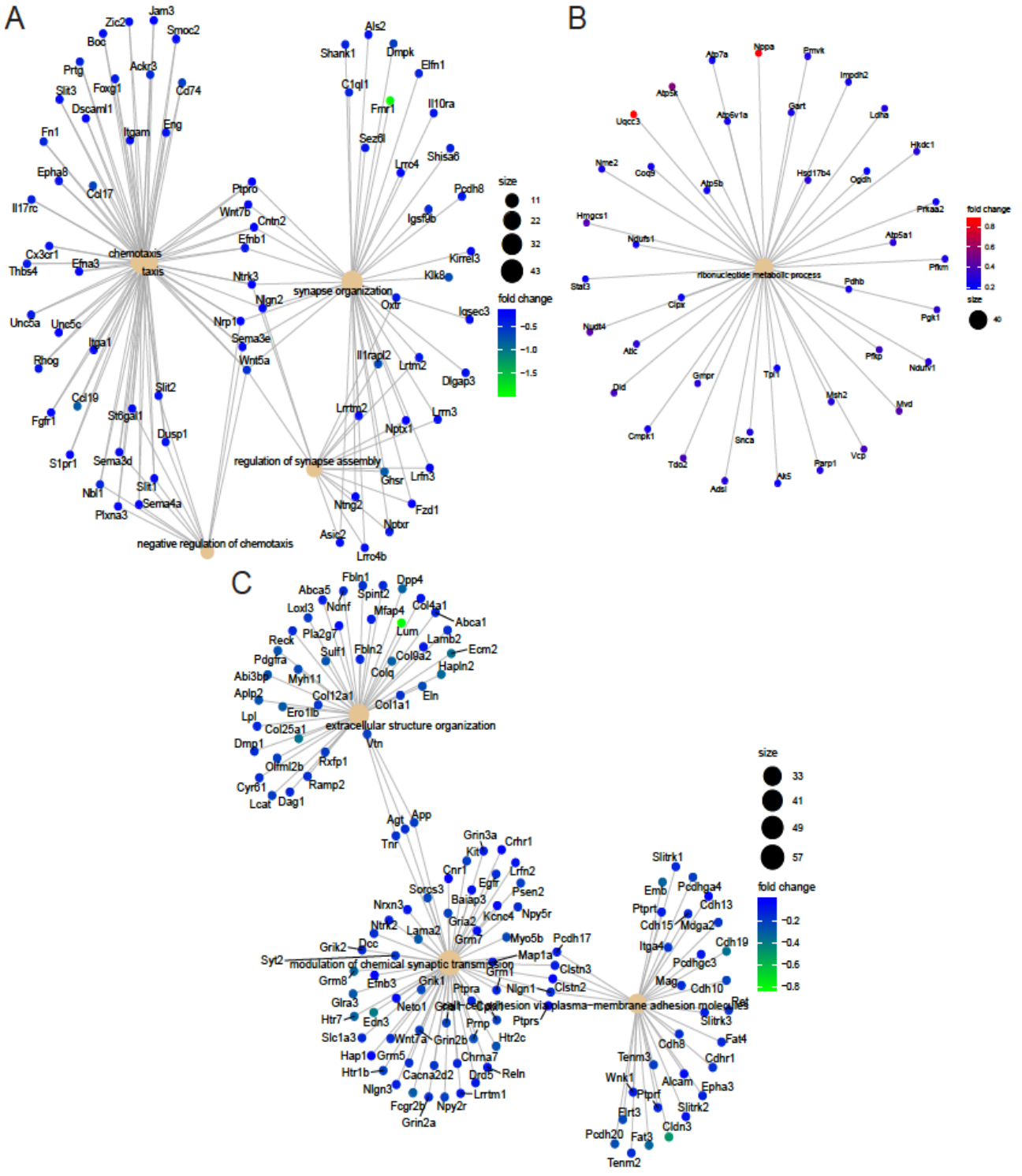
A
chemotaxis
taxis
synapse organization
regulation of synapse assembly
negative regulation of chemotaxis
size
fold change
B
ribonucleotide metabolic process
fold change
size
C
extracellular structure organization
modulation of chemical synaptic transmission
cell-cell adhesion via plasma-membrane adhesion molecules
size
fold change

Figure S1. Clustering of RNAs with changes in TE and mRNA abundance to identify functional hubs (Related to Figure 1, also see TableS1)

(A) Network clustering of "mRNA up" RNAs from the ribosome profiling and RNA-seq in WT and *Fmr1* KO hippocampus. Nodes indicate the functional processes linked to the RNAs identified. Fold changes are indicated.

(B) Network clustering of the functional processes in the "mRNA down" RNAs

(C) Network analysis of the of the functional processes in the "TE down" mRNAs

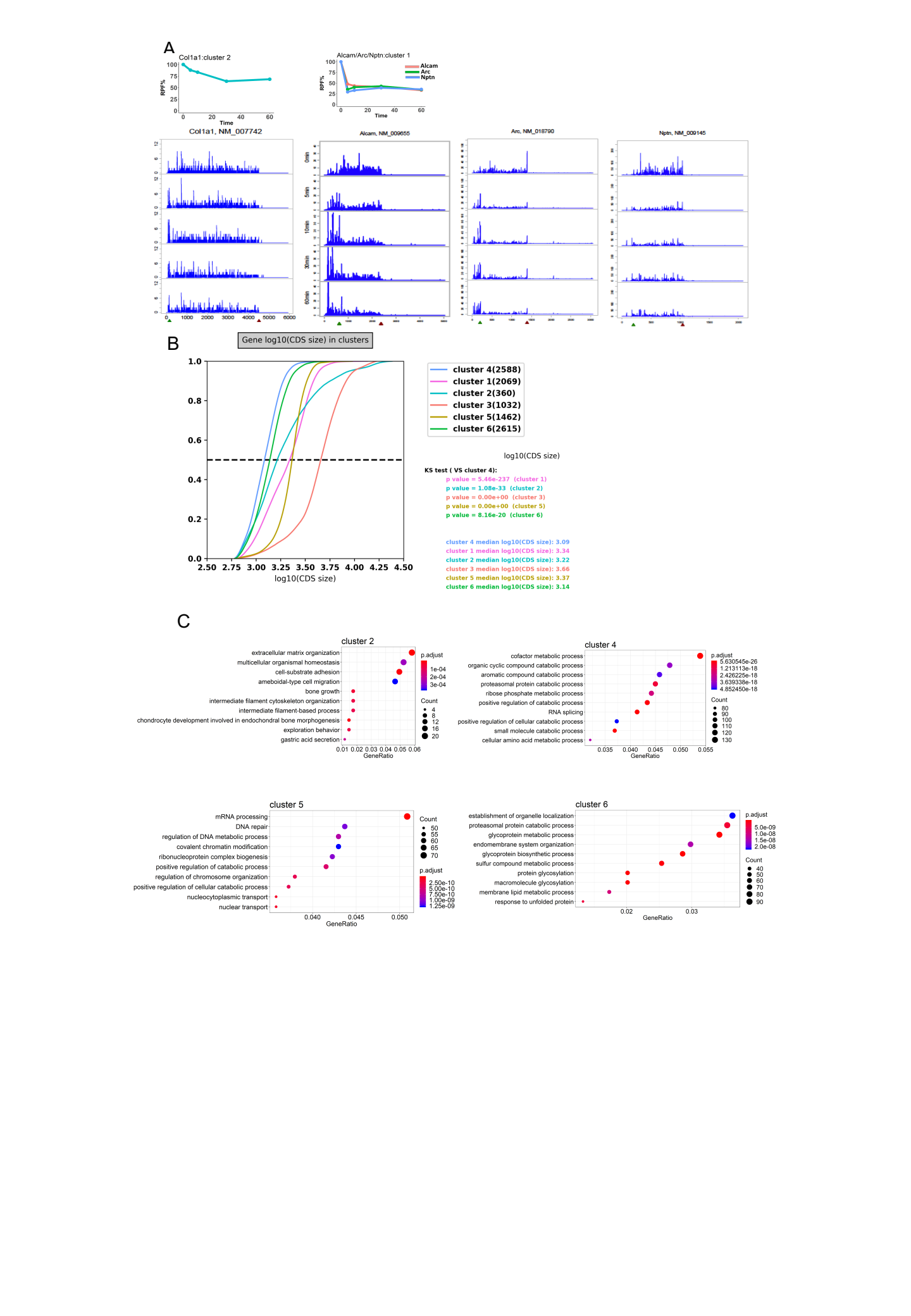
A
Col1a1:cluster 2
Alcam/Arc/Nptn:cluster 1
Alcam
Arc
Nptn
RPF%
Time
Col1a1, NM_007742
Alcam, NM_009655
Arc, NM_018790
Nptn, NM_009145
0min
5min
10min
30min
60min
B
Gene log10(CDS size) in clusters
cluster 4(2588)
cluster 1(2069)
cluster 2(360)
cluster 3(1032)
cluster 5(1462)
cluster 6(2615)
log10(CDS size)
KS test (VS cluster 4):
p value = 5.46e-237 (cluster 1)
p value = 1.08e-33 (cluster 2)
p value = 0.00e+00 (cluster 3)
p value = 0.00e+00 (cluster 5)
p value = 8.16e-20 (cluster 6)
cluster 4 median log10(CDS size): 3.09
cluster 1 median log10(CDS size): 3.34
cluster 2 median log10(CDS size): 3.22
cluster 3 median log10(CDS size): 3.66
cluster 5 median log10(CDS size): 3.37
cluster 6 median log10(CDS size): 3.14
C
cluster 2
extracellular matrix organization
multicellular organismal homeostasis
cell-substrate adhesion
ameboidal-type cell migration
bone growth
intermediate filament cytoskeleton organization
intermediate filament-based process
chondrocyte development involved in endochondral bone morphogenesis
exploration behavior
gastric acid secretion
p.adjust
Count
GeneRatio
cluster 4
cofactor metabolic process
organic cyclic compound catabolic process
aromatic compound catabolic process
proteasomal protein catabolic process
ribose phosphate metabolic process
positive regulation of catabolic process
RNA splicing
positive regulation of cellular catabolic process
small molecule catabolic process
cellular amino acid metabolic process
cluster 5
mRNA processing
DNA repair
regulation of DNA metabolic process
covalent chromatin modification
ribonucleoprotein complex biogenesis
positive regulation of catabolic process
regulation of chromosome organization
positive regulation of cellular catabolic process
nucleocytoplasmic transport
nuclear transport
cluster 6
establishment of organelle localization
proteasomal protein catabolic process
glycoprotein metabolic process
endomembrane system organization
glycoprotein biosynthetic process
sulfur compound metabolic process
protein glycosylation
macromolecule glycosylation
membrane lipid metabolic process
response to unfolded protein

Figure S2. Run-off ribosome profiling of WT mouse hippocampal slices. (Related to Figure 3, also see Table S1)

(A) Ribosome runoff patterns for clusters 1 and 2. The RPFs of each gene at each time point was normalized to time 0. The euclidean distance matrix was then calculated, followed by hierarchical clustering using Ward's agglomeration method (Ward, 1963). The global pattern of each sub-cluster was summarized using the corresponding median and standard deviation in each timepoint. Representative ribosome runoff profiles are shown.

(B) CDS length dependency of the ribosome runoff rates. Results of the K-S test for significance are shown

(C) GO terms for sub-clusters 2,4, 5 and 6.

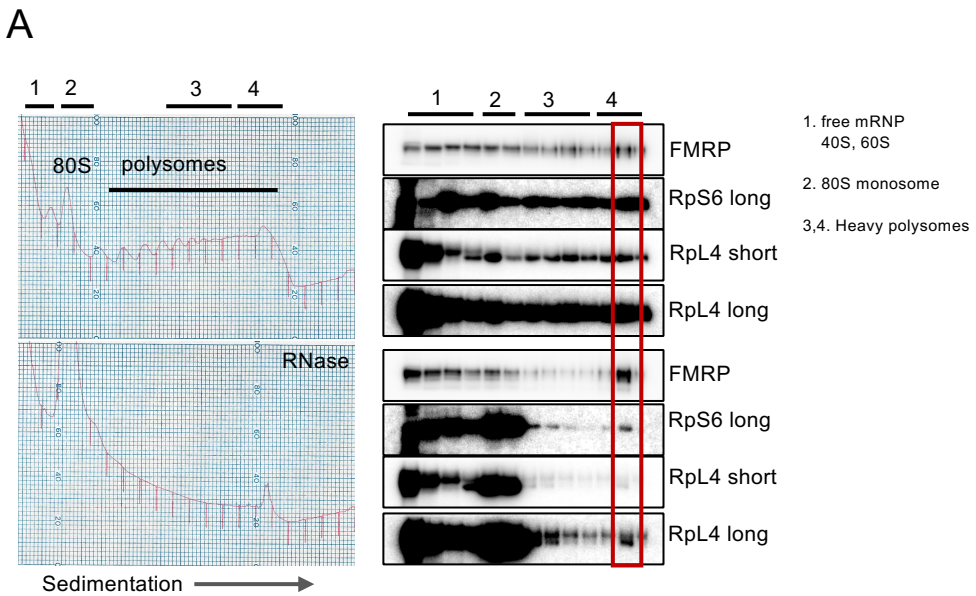
A
1
2
3
4
80S
polysomes
RNase
Sedimentation
FMRP
RpS6 long
RpL4 short
RpL4 long
1. free mRNP
40S, 60S
2. 80S monosome
3,4. Heavy polysomes

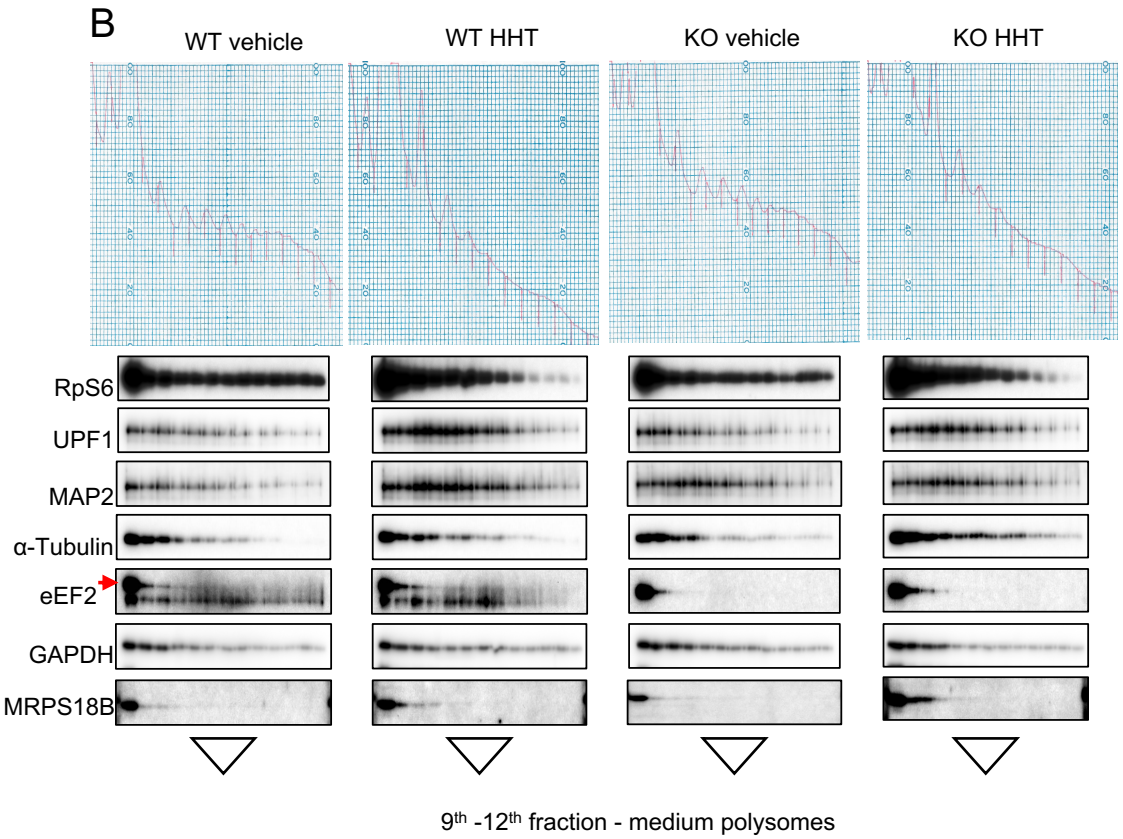
B
WT vehicle
WT HHT
KO vehicle
KO HHT
RpS6
UPF1
MAP2
α-Tubulin
eEF2
GAPDH
MRPS18B
9th -12th fraction - medium polysomes

Figure S3. Sedimentation of proteins in polysome sucrose gradients. (Related to Figure 4, also see Table S1)

(A) Hippocampal extracts, some of which were treated with RNAse A, were centrifuged through sucrose gradients, fractionated, and immunoblotted for FMRP, RPS6 and RPL4. Long and short refer to relative exposure times.

(B) Hippocampal slices from WT or FMRP KO mice were treated with vehicle only or HHT for 30 min. The gradients were fractionated and immunoblotted for the indicated proteins. The red arrow denotes the eEF2 band. The medium polysome fractions are indicated.

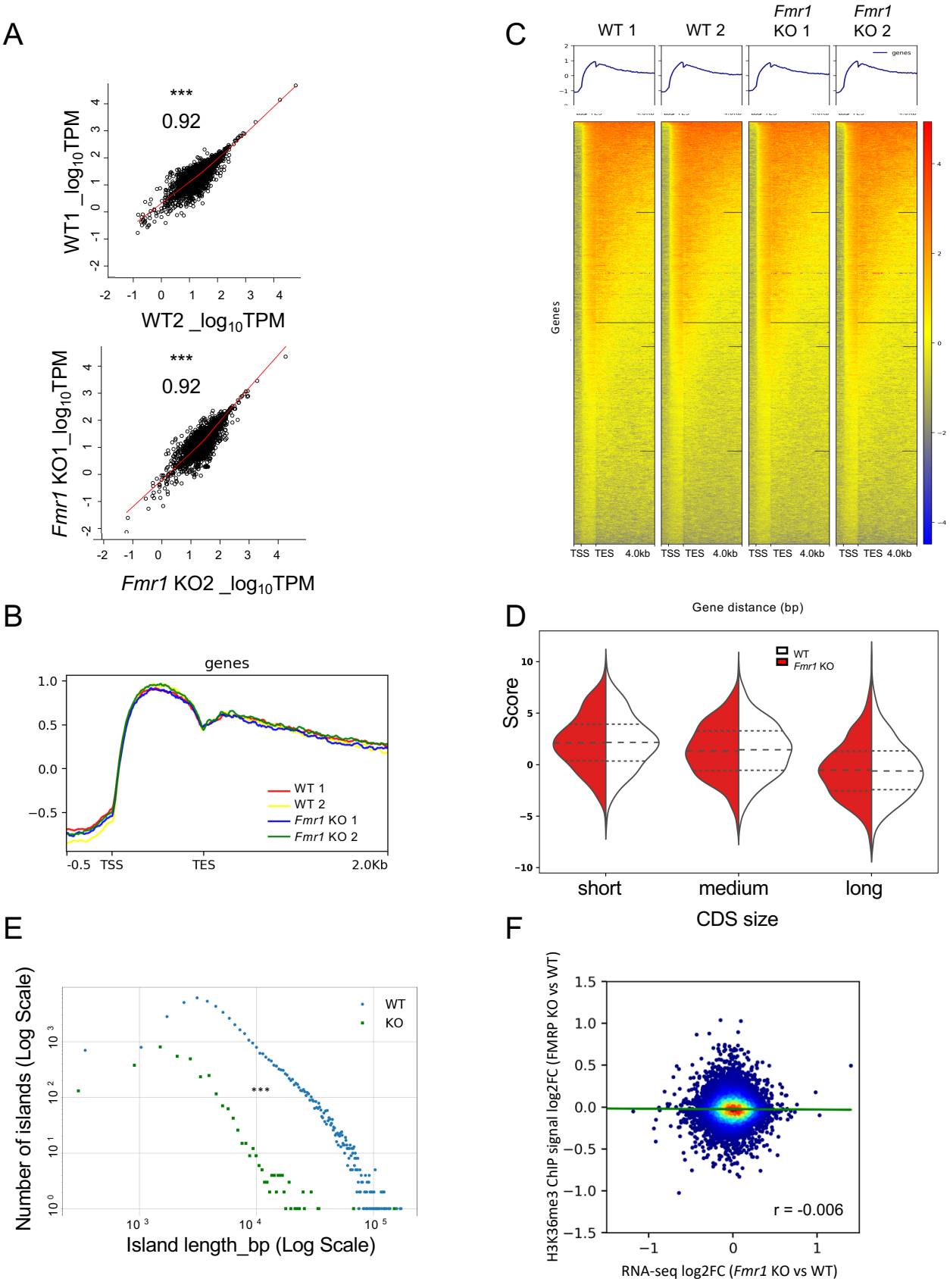
A
***
0.92
WT1 _log10TPM
WT2 _log10TPM
***
0.92
Fmr1 KO1 _log10TPM
Fmr1 KO2 _log10TPM
B
genes
WT 1
WT 2
Fmr1 KO 1
Fmr1 KO 2
-0.5 TSS
TES
2.0Kb
C
WT 1
WT 2
Fmr1 KO 1
Fmr1 KO 2
genes
Genes
TSS TES 4.0kb
D
Gene distance (bp)
WT
Fmr1 KO
Score
short
medium
long
CDS size
E
WT
KO
***
Number of islands (Log Scale)
Island length_bp (Log Scale)
F
H3K36me3 ChIP signal log2FC (FMRP KO vs WT)
r = -0.006
RNA-seq log2FC (Fmr1 KO vs WT)

Figure S4. H3K36me3 ChIP metagene analysis (Related to Figure 6, also see Table S2)

(A) Scatter plot for ChIP-seq normalized reads density (Transcripts per million mapped reads, TPM) mapped to the genic regions between biological replicate samples, WT1 and WT2 and *Fmr1* KO1 and *Fmr1* KO2. Pearson r values for correlation efficiency are shown. Asterisks indicate statistical significance.

(B) Metagene plots using deepTools (Ramírez et al., 2016) for distribution of H3K36me3 marks along the gene lengths. A similar increase in ChIP signal in all samples is seen in the gene body. The transcription start site (TSS), Transcription end site (TES) and 2.0kb downstream is shown.

(C) Heatmap for distribution of H3K36me3 signal along the gene length in each sample, compiled plot in Figure S4B. The transcription start site (TSS), Transcription end site (TES) and 4.0kb downstream is shown. No overall differences in ChIP signal was observed between samples.

(D) Violin plot to assess the effect of gene length on H3K36me3 ChIP signal between WT (white) and *Fmr1* KO (red) samples.

(E) Histogram depicting number of islands (log scale) and their respective island length for all significant islands (bp in log scale) identified in the WT (blue) and *Fmr1* KO (green) ChIP-seq. The island lengths were parsed in bins of 100bp and the center of each bin is plotted in the histogram. Asterisks indicate statistical significance.

(F) Scatter plot comparing the $\log_2$FC in RNA-seq (x-axis) with the ChIP-seq data (y-axis) averaging H3K36me3 island differences within each gene is plotted. Pearson correlation coefficient value is stated.

A

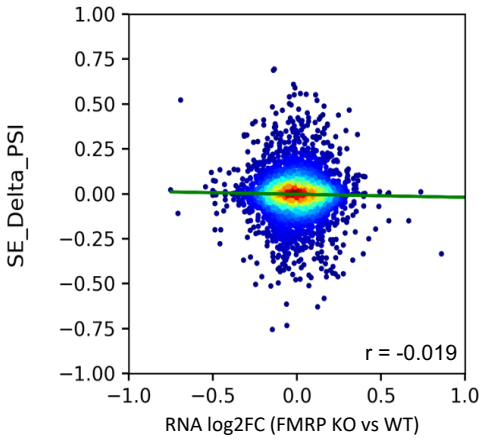
SE_Delta_PSI
RNA log2FC (FMRP KO vs WT)
r = -0.019

B

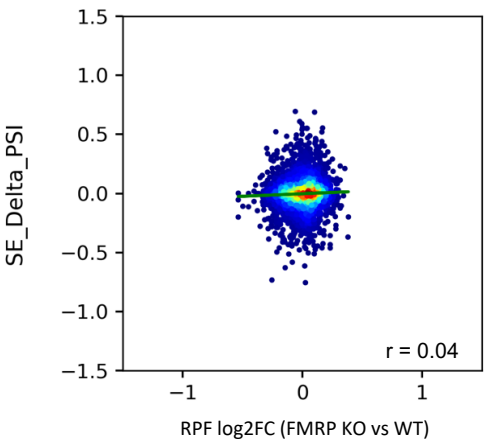
SE_Delta_PSI
RPF log2FC (FMRP KO vs WT)
r = 0.04

C

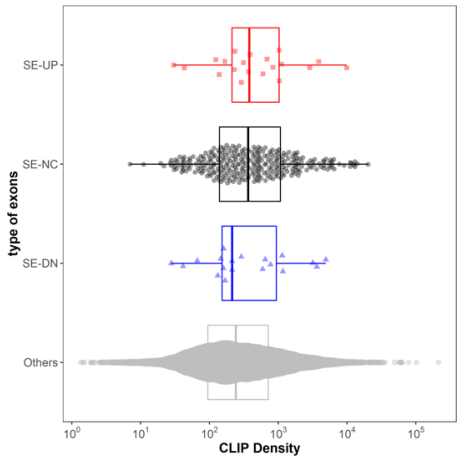
SE-UP
SE-NC
SE-DN
Others
type of exons
CLIP Density

D

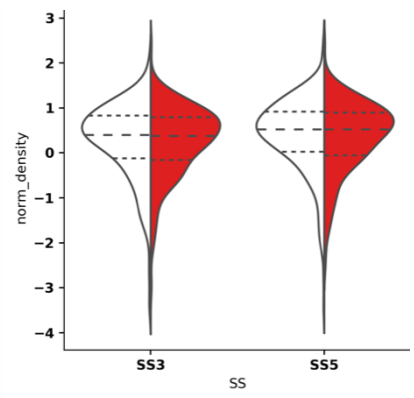
norm_density
SS3
SS5
SS

+/-150nt

E

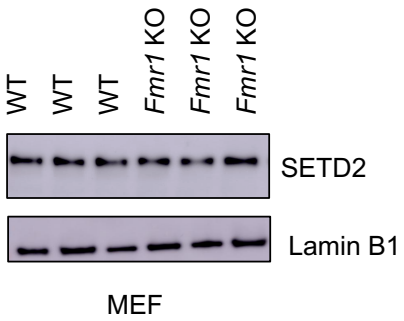
WT
WT
WT
Fmr1 KO
Fmr1 KO
Fmr1 KO
SETD2
Lamin B1
MEF

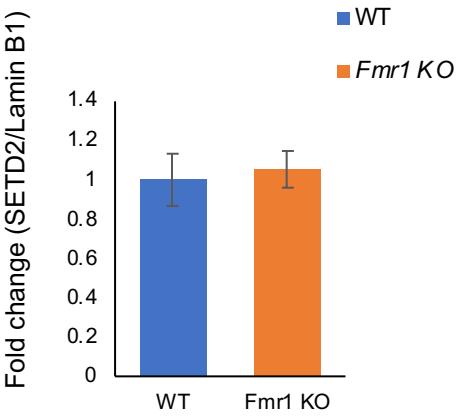
WT
Fmr1 KO
Fold change (SETD2/Lamin B1)
WT
Fmr1 KO

Figure S5. Comparison of skipped exon genes to RNA abundance and RPF levels (Related to Figure 1,6, and 7 also see Table S1 and S3)

(A) Scatter plot for the delta percent spliced-in (Psi/Ψ) score of skipped exons (y-axis) (From Figure 7) versus their RNA fold changes (From Figure 1) on the x axis. Pearson correlation coefficient value is stated.

(B) Scatter plot for the delta percent spliced-in (Psi/Ψ) score of skipped exons (y-axis) (From Figure 7) versus their RPF levels (From Figure 1) on the x axis. Pearson correlation coefficient value is stated.

(C) Swarm plots are shown representing the FMRP CLIP density (CLIP level/length) using the FMRP CLIP-Seq data (GSE45148) at skipped exons and their flanking introns of genes with increased exon skipping (SE-UP in red), decrease skipped exons SE-DN in blue) and no significant change in skipped exons (SE-NC) are plotted. The other category represents exons with no alternative splicing detected. Wilcoxon test was used to determine significance of differences amongst the categories.

(D) Violin plot for the H3K36me3 ChIP signal +/-150nt at the 5' (SS5) and 3' (SS3) splice sites of the alternatively skipped exons in WT (white) and *Fmr1* KO (red) hippocampus tissue (p-value<0.05, Wilcox test for significance). Also see Figure 7F.

(E) Western blot analysis of SETD2 and Lamin B1 in immortalized MEFs from WT and *Fmr1* KO mice (left), passage number 31. When quantified and made relative to Lamin B1 (right), there was no observable change in SETD2 levels in the *Fmr1* KO (3 replicates, p=0.48, two-tailed t test). Error bars represent the S.E.M (also see Figure 5)